minerals

Article

Integration of Stress–Strain Maps in Mineral Systems Targeting for IOCG Mineralisation within the Mt. Woods Inlier, Gawler Craton, South Australia

Jonathan Nicholas Gloyn-Jones [1,*], Ian James Basson [1,2], Ben Stoch [1], Corné Koegelenberg [1,2] and Michael-John McCall [1]

[1] Tect Geological Consulting, Unit 3 Metrohm House, Gardner Williams Avenue, Paardevlei 7130, South Africa; ianbasson@tect.co.za (I.J.B.); benstoch@tect.co.za (B.S.); cornekoegelenberg@tect.co.za (C.K.); michaelmccall@tect.co.za (M.-J.M.)
[2] Department of Earth Sciences, Stellenbosch University, Private Bag X1, Matieland 7602, South Africa
* Correspondence: jonathangloyn-jones@tect.co.za

Abstract: The application of finite element analysis is used to simulate the relative distribution and magnitude of stress–strain conditions during a geologically brief, NNW-SSE-oriented, extensional event (1595 Ma to 1590 Ma), co-incident with IOCG-hydrothermal fluid flow and mineralisation across the Mt Woods Inlier, Gawler Craton, South Australia. Differential stress and shear strain maps across the modelled terrane highlight regions that were predisposed to strain localization, extensional failure and fluid throughput during the simulated mineralisation event. These maps are integrated with other datasets and interpretation layers, one of which is a proposed structural–geometrical relationship apparent in many world-class IOCG deposits, including Prominent Hill, Olympic Dam, Sossego, Salobo, Cristalino and Candelaria. These deposits occur at steeply plunging, pipe-like intersections of conjugate extensional systems of faults, shears and/or contacts, wherein the obtuse angle may have been bisected by the maximum principal extensional axis (viz., σ_3) during mineralisation. Several other layers are also used for the generation of targets, such as distance from major shear zones, favourable host lithologies, and proximity to tectonostratigraphic contacts of markedly contrasting competency. The result is an integrated target index or heat map for IOCG prospectively across the Mt. Woods Inlier.

Keywords: structural control; fluid flow; IOCG mineralisation; finite element analysis; numerical modelling; exploration; target generation; Mt. Woods Inlier; Gawler Craton

check for updates

Citation: Gloyn-Jones, J.N.; Basson, I.J.; Stoch, B.; Koegelenberg, C.; McCall, M.-J. Integration of Stress–Strain Maps in Mineral Systems Targeting for IOCG Mineralisation within the Mt. Woods Inlier, Gawler Craton, South Australia. *Minerals* **2022**, *12*, 699. https://doi.org/10.3390/min12060699

Academic Editor: Paul Alexandre

Received: 10 March 2022
Accepted: 18 May 2022
Published: 31 May 2022

1. Introduction

The discovery of near-surface, world-class deposits is becoming sporadic, with an increasing focus on deeper-seated orebodies situated in more structurally complex terranes [1,2]. The development of improved critical detection technologies and integrated conceptual targeting methodologies, e.g., [2] are two ways to address this. Both require a robust understanding of the structural controls of mineralisation, including the characteristics of the deposit, emplacement style, age, origin [3] and the mechanisms of, for instance, breccia and vein formation in the context of regional tectonism and deformation events [4].

It is widely accepted that the formation of hydrothermal mineral deposits is governed by the interaction of structural–geometrical, hydrological, thermal and chemical controls, e.g., [5–12]. Understanding the structural–geometrical controls is critical in establishing pathways or conduits to reservoirs at both the deposit scale and the regional scale, e.g., [6]. The manner in which structural–geometrical elements influence and control the development and geometry of orebodies and ore-shoots has been demonstrated for a wide range of deposit types and tectonic settings, e.g., [13–21]. On a deposit scale, controlling structural elements include tectonostratigraphic contacts, fault networks, shear zones and folds that are active within a particular kinematic framework or during a particular deformation event, thereby presenting sites of preferential or directional permeability, dilation, hydrothermal fluid throughput and consequently mineralisation.

Fluid flow is an integral part of hydrothermal mineralisation [22–24]. A full hydrodynamic study analyses the driving forces, fluid pressure regimes, fluid flow rates and direction, and their relationships with mineralisation loci. Driving forces of fluid flow may be related to fluid overpressure, topographic relief, tectonic deformation and/or fluid density changes [22,24,25]. An important consideration is whether structural controls of mineralisation and fluid flow are "passive"—attributable to structures developed before mineralisation—or "active", i.e., related to structures which evolved during mineralisation [3]. In the case of active controls, thermo-baric conditions, the presence and nature of fluids, and stress state are closely related to ore-forming processes.

IOCG mineralisation is closely associated with the development of Cu-Au-rich, polymetallic, haematitic breccia complexes that are formed by numerous phases of multi-stage hydrothermal brecciation, pervasive replacement and cataclastic milling, e.g., [26–28], either along or at the intersection of faults and/or at lithological contacts, testifying to the structurally controlled discharge of large amounts of fluids. IOCG-related or polymetallic mineralisation within the Mt. Woods Inlier is situated along four well developed, deep-seated shear zone networks and/or structural corridors, including the Southern Overthrust, Skylark Shear Zone, Jupiter Shear Zone and Cairn Hill Shear Zone (Figure 1. The overwhelming concentration of IOCG-related occurrences, prospects and deposits occur along the southern extent of the NW-SE-trending Southern Overthrust and Skylark Shear Zone (Figure 1).

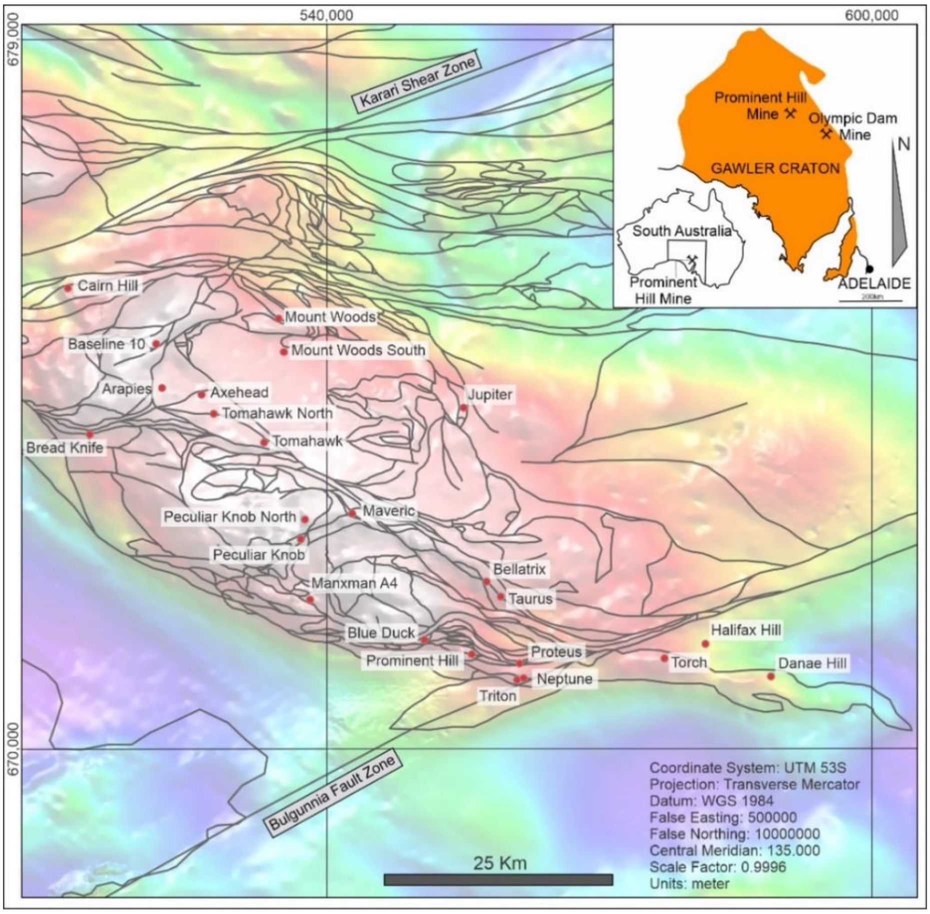

Figure 1. Overview of the Mt. Woods Inlier illustrating the locations of prospects and deposits across the region. The base map is total gravity, which highlights a sigmoidal zone between two ENE-

trending, left-lateral shear zones (Karari and Bulgunnia Shear/Fault Zones). Cu and polymetallic mineralisation occurs up to 22 km from the Bulgunnia Fault Zone, with Prominent Hill occurring 6 km from this structure. In a similar mode, Cairn Hill occurs 7 km south of the Karari Shear Zone, with several other polymetallic deposits and occurrences within 22 km north of the Karari Shear Zone (Ramsey (Fe); Injabreck (Cu-Ba-Ce-Th-Be-REE), outside of the frame of the figure). Coordinate system and projection is consistent throughout the paper.

Hydrothermal fluid flow (Fe, Cu, U and Au) is interpreted to have been active during a brief, transient extensional event (1595 Ma to 1590 Ma) across almost the entire terrane, e.g., [29–31]. This short-lived mobilization event is interpreted to reflect either NE-SW-oriented extension [29,32] or NNW-SSE-oriented extension [30,33].

This contribution presents a workflow for the application of finite element analysis to simulate the stress–strain state and, as a proxy, the theoretical, deformation-induced fluid flow across the Mt. Woods Inlier. Other interpretation layers include a proposed structural–geometrical control of polymetallic IOCG-style mineralisation that occurs globally. These layers are integrated into a conceptual targeting methodology for IOCG-style hydrothermal mineralisation within structurally complex terranes.

2. Regional Geological Setting

The tectonic evolution and geological architecture of the Gawler Craton, described by [29], builds on previous observations and models, e.g., [34–37]. The craton comprises an extensive, but poorly exposed, Archean to Neoproterozoic terrane, overlain by Paleoproterozoic volcano-sedimentary cover sequences, which underwent major tectonic reworking and magmatic events during the Sleafordian Orogeny (2465–2410 Ma), Kimban Orogeny (1740–1690 Ma), Kararan Orogeny (1610/1575–1540/1530 Ma) and the overlapping Olarian Orogeny (1600–1500 Ma), e.g., [29,38–42]. The Gawler Craton may be subdivided into fourteen domains, based on tectono-stratigraphic and geophysical attributes, e.g., [35,36,43], including the Mt. Woods Inlier [44–51], which essentially comprises a rhomboidal-shaped domain bounded by two major ENE-trending shear zone corridors (Figure 1).

Despite the scarcity of outcrop throughout the domain, due to thick cover, several studies have characterized its lithostratigraphic inventory, tectonothermal evolution and internal structure, e.g., [32,35,46,48,52,53]. The lithostratigraphy has been previously defined as the Mt. Woods Complex [48], consisting of a variety of sporadically outcropping, supracrustal, granitic to gabbroic units [35,48] that exhibit greenschist to granulite facies metamorphism, and structures that exhibit poly-deformed ductile to brittle deformation, e.g., [32,46,48,50,52,53]. Supracrustals, termed the Skylark Metasediments, consist of a variety of banded iron formation (BIF), metapsammite and metapelitic units, quartz–feldspar–biotite schist, gneissic calc-silicates and quartzofeldspar granofels, tentatively related to the Hutchison Group [32,52,54,55]. Metamorphosed supracrustals were intruded by the syntectonic Engenina Adamellite (1692 $\pm$ 25 Ma) and the post-tectonic Balta Granite Suite (1584 $\pm$ 18 Ma), which is equivalent to the Hiltaba Granite Suite in the southern and central parts of the Gawler Craton [35,56].

The Mt. Woods Inlier has experienced high-temperature, low-pressure, prograde metamorphism, wherein units in its southern portions have experienced greenschist to lower-amphibolite-grade metamorphism, e.g., [57], while the central and northern portions are dominated by units that show much higher grades, up to granulite facies (P up to 4.7 kbar, T up to 550–750 °C), e.g., [32,48,50,52,53].

The structural evolution of the Mt. Woods Inlier [35,46] has been described in terms of two well-constrained deformational phases (D_1–D_2) and several relatively uncharacterized deformational phases (D_3–D_5). The earliest deformation event (D_1) is defined by the development of a bedding (S_0)-parallel foliation with the preferred orientation of biotite, sillimanite and quartz–feldspar aggregates and an axial planar gneissic foliation, denoted S_1, that formed during tight to isoclinal folding (F_1) during high-T, upper amphibolite to granulite facies metamorphism at 1736 ± 13 Ma and attributed to the onset and early stages of the Kimban Orogeny between 1740 and 1690 Ma [35,44–46,58].

D_2 is characterized by a subsequent episode of pervasive, open to isoclinal folding (F_2) [46], consistent with syntectonic intrusion of the Engenina Adamellite (1692 ± 25 Ma) [35,56] during N-S shortening, and attributed to the latter stages of the Kimban Orogeny [46]. The definition of post-D_2 deformation remains a contentious issue as, although these clearly overprint the Engenina Adamellite, there are no outcrops that definitively elucidate the temporal association between structures [46].

The structural interpretation of the Mt. Woods Inlier after [32] builds on observations and interpretations initially presented by [46,50], elucidating the subdivision of the inlier into discrete geophysical zones separated by large-scale fault/shear zone systems. The geometry and extent of these NE-SW- and ESE- to SE-trending faults and/or shear zone corridors overprint D_2 structures and fabrics, observable both in outcrop pavements and definable from aeromagnetic surveys, e.g., the Spire Shear Zone, Moonlight Shear Zone, Cairn Hill Shear Zone, Panorama Shear Zone, Skylark Shear Zone, Karari Shear Zone, Bulgunnia Fault Zone and the Southern Overthrust [32,35,46,50].

The activation of these structures during D_3 reflects burial and high-T/low-P metamorphism of the Coodnambana Metaconglomerate (1595 ± 10 Ma), coincident with IOCG-related mineralisation throughout the Olympic Dam IOCG Province and the emplacement of several magmatic suites, including the late syn-, to post-tectonic Balta Granite Suite (~1584 ± 18 Ma) (Hiltaba Granite Suite equivalent) and the Gawler Range Volcanics (~1592 ± 3 Ma), during the Kararan Orogeny [29,30,35,46,48–51,56,58,59].

Ages from IOGC-related hydrothermal zircons and magmatic zircons are almost identical, suggesting that IOCG-related hydrothermal alteration and mineralisation immediately followed magma emplacement and subsequent cooling [49,60]. Hydrothermal fluid flow (accompanied by Fe, Cu, U and Au) is interpreted to have been active during a brief extensional event (1595 Ma to 1590 Ma) across almost the entire terrane, e.g., [29–31]. This short-lived, transient mobilization event is interpreted to have responded to—or to reflect—either NE-SW-oriented extension [29,32] or NNW-SSE-oriented extension [30,33].

3. Geophysical Data Interpretation

Aeromagnetic and Bouguer gravity datasets used for the structural re-interpretation of the Mt. Woods Inlier were sourced from the South Australian Resource Information Gateway (SARIG) (https://map.sarig.sa.gov.au/ (accessed on 27 February 2019)). These data sets include Total Magnetic Intensity (TMI), TMI Reduced to Pole (TMI_RTP), TMI_RTP 1st Vertical Derivative (TMI_RTP_VD1) and Gravity (WPA-SGRV-EGP) datasets (Figure 2). TMI datasets have a survey height of approximately 80 m above ground and are gridded to a resolution of 100 m.

3.1. Structural Re-Interpretation of the Mt. Woods Inlier

The general principals outlined in [61–63] were followed in the re-interpretation of available geophysical data datasets. During initial stratigraphic form line and fault mapping, image combinations were used to highlight and manually digitize continuous and discontinuous linear to sub-linear features, interpreted as bedding, structural fabrics (foliation) and lithological contacts, which are often offset or rotated against structural discontinuities that include faults, shear zones and dykes.

Several overlain combinations of TMI derivatives (e.g., VD and RTP) were used to highlight and discretise domains of homogeneous magnetic intensity and texture (Figure 3). These domains were correlated to known or mapped regional lithological units and classified accordingly, in the form of a “proxy” geological map (Figure 3).

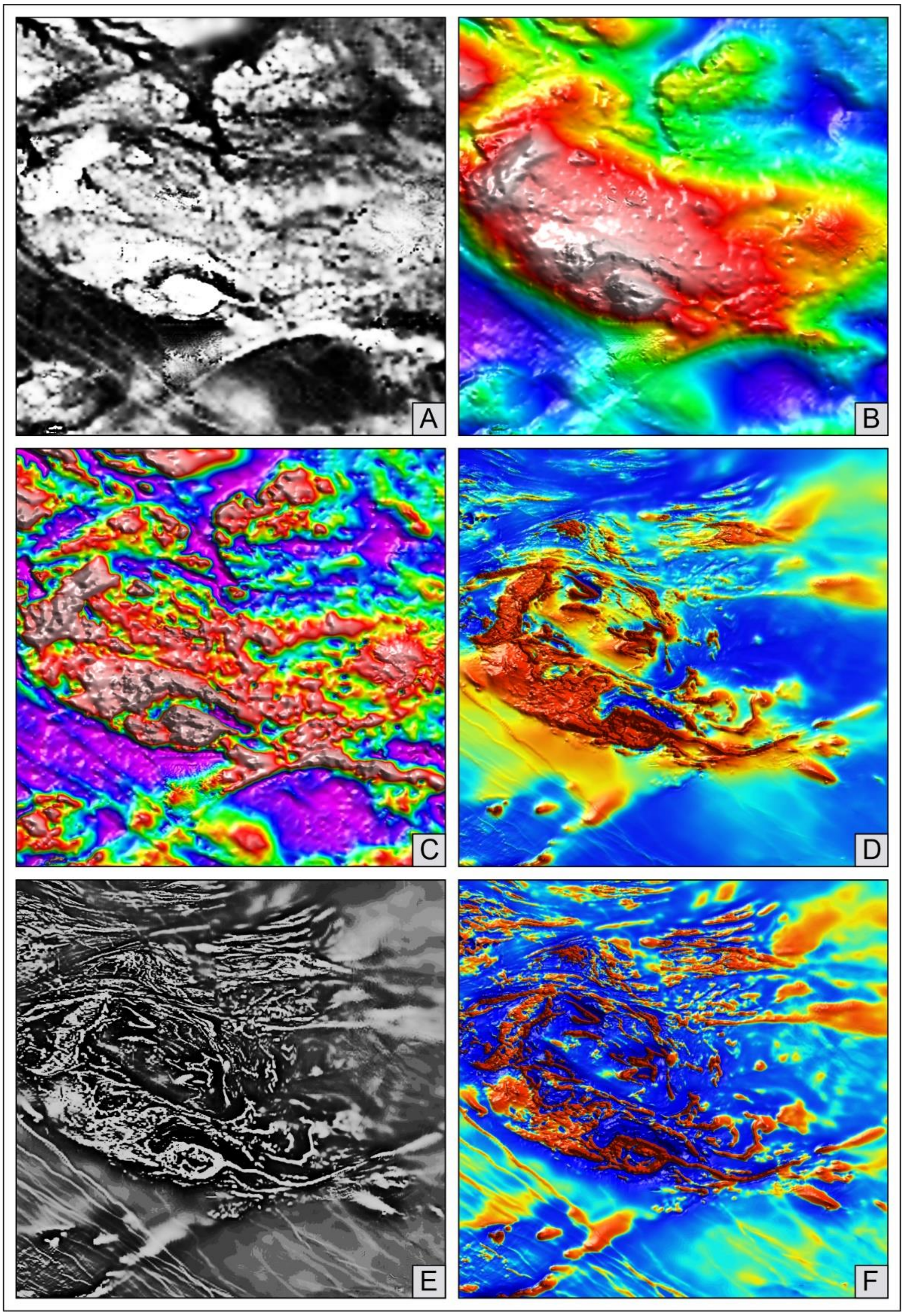

Figure 2. Aeromagnetic and Bouguer gravity datasets used for the structural re-interpretation of the Mt. Woods Inlier (https://map.sarig.sa.gov.au/ (accessed on 27 February 2019)). (**A**) Gravity (WPA-SGRV-EGP) 1st Vertical Derivative; (**B**) Gravity (WPA-SGRV-EGP); (**C**) Gravity UC1000 Residual (WPA-SGRV-EGP); (**D**) Total Magnetic Intensity (TMI); (**E**) TMI Reduced to Pole (RTP) 1st Vertical Derivative; (**F**) TMI RTP UC1000.

The structural interpretation primarily focused on major structures, principally shears and shear zones, many of which coincide with lithological and/or domain contacts (Figures 3 and 4). The result is a re-interpreted structural architecture and geological domaining of the Mt. Woods Inlier, which is amenable to finite element analysis. This overlaps with and refers to previous interpretations, e.g., [32,35,46,50,64–72].

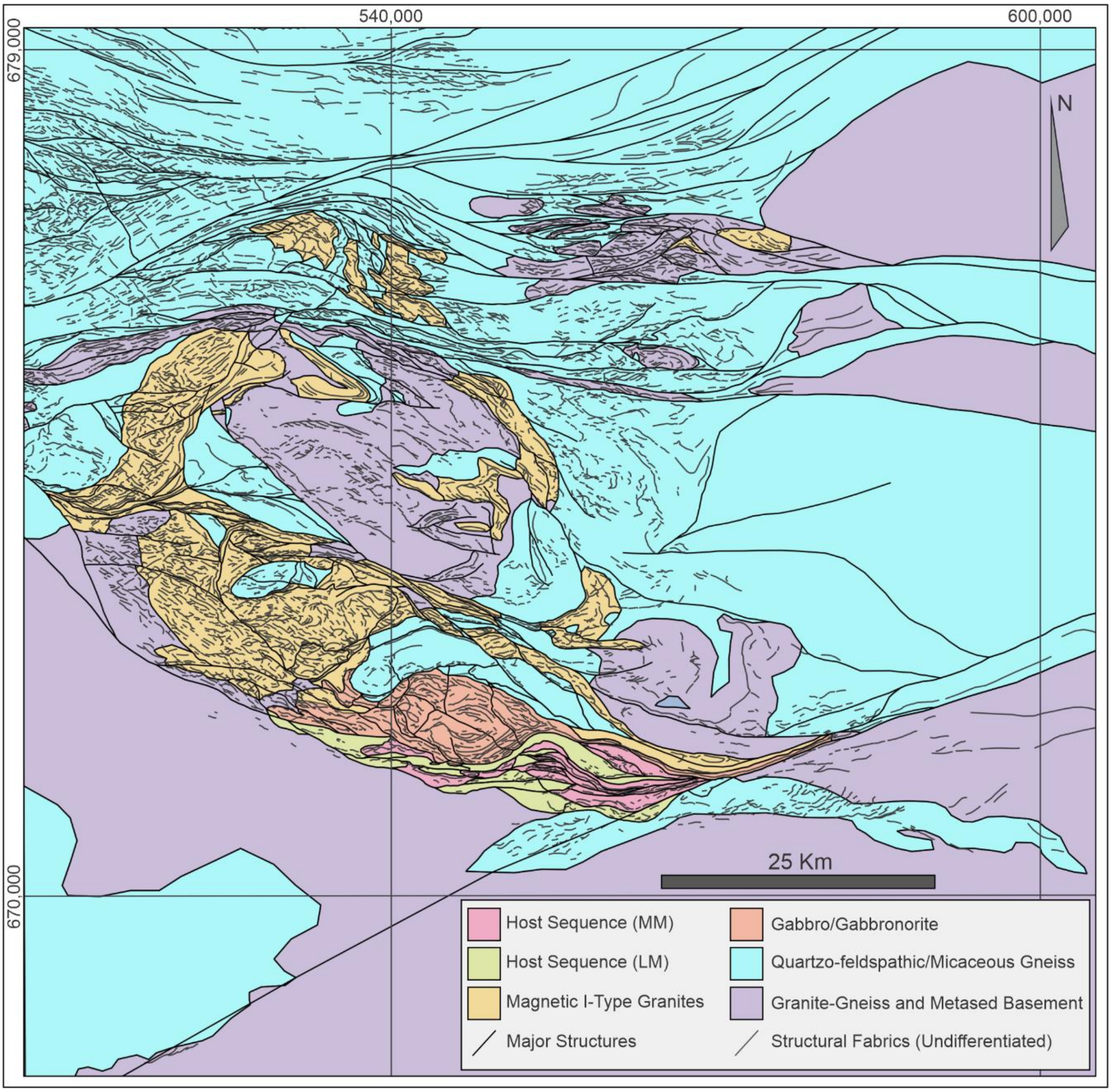

Figure 3. Structural and lithological re-interpretation of the Mt. Woods Inlier. Lithological classification broadly follows that of [68].

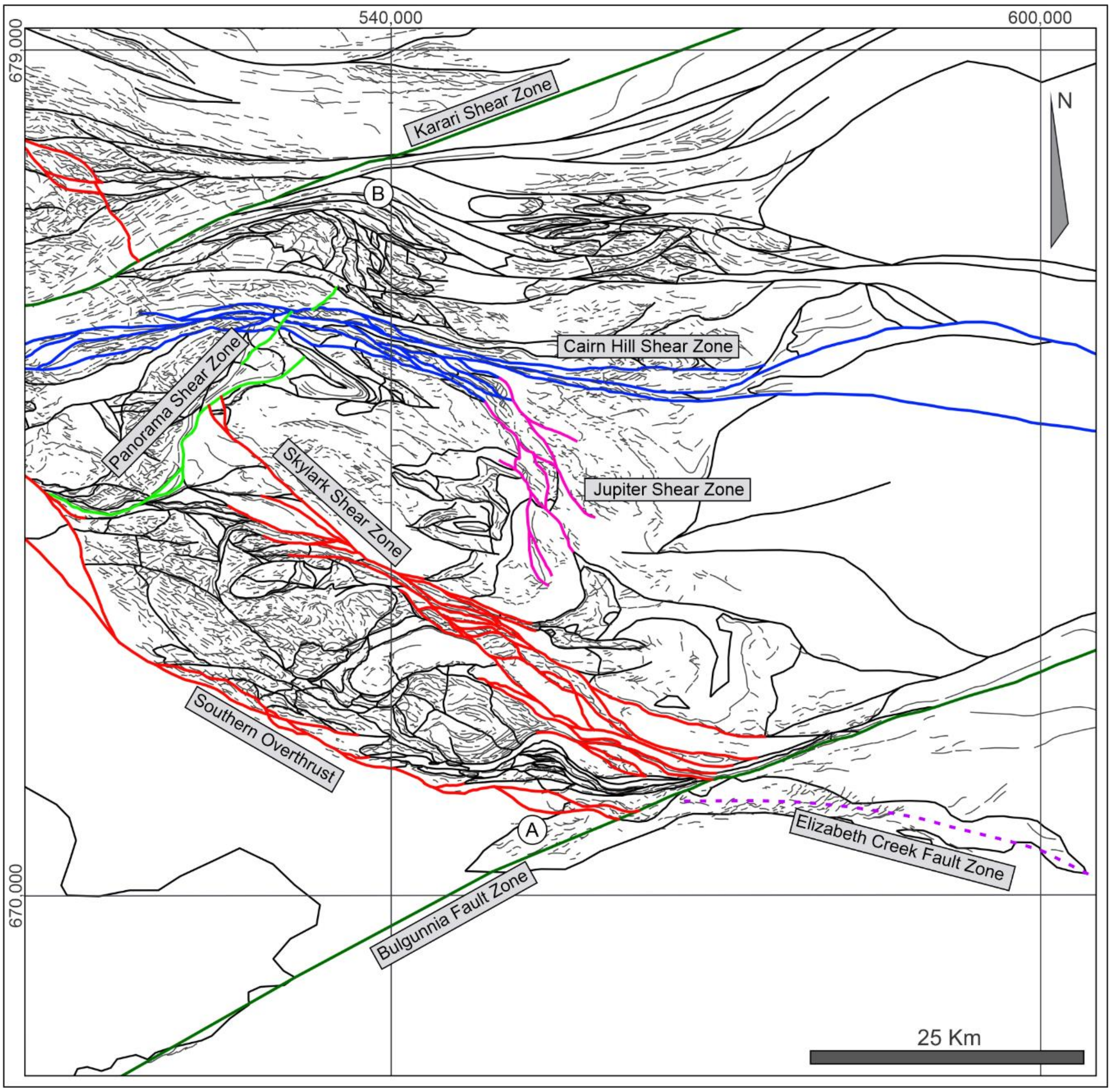

Figure 4. Structural architecture of the Mt. Woods Inlier with highlighted deep-seated lithospheric-scale structures, including the Karari Shear Zone, Bulgunnia Fault Zone, Elizabeth Creek Fault Zone, Jupiter Shear Zone, Skylark Shear Zone, Southern Overthrust, Panorama Shear Zone and Cairn Hill Shear Zone.

3.2. Description and Insights

The Mt. Woods Inlier essentially comprises a sigmoidal-shaped block or domain defined by high magnetic responses and gravity anomalies (Figures 1 and 2). It is bounded on its southern and northern flanks by two major, ENE-trending shear zones, termed the Karari and Bulgunnia Shear/Fault Zones (Figures 1 and 4). These bounding structural corridors are interpreted as first-order, deep-seated, lithospheric-scale structures, a concept supported by interpreted seismic lines [73].

The curvature of deflected, interleaved tectonostratigraphy, adjacent to the shear zones at points A and B (Figure 4), suggest a cumulative left-lateral or sinistral sense of movement along the Karari and Bulgunnia Shear/Fault Zones. The western boundary of the inlier, well-defined by a sharp discontinuity in magnetic and gravity signatures, commonly known as the Southern Overthrust and/or Fitzgerald Shear and/or an extension of the Elizabeth Creek Fault Zone, exhibits a NW-SE-trending, sigmoidal (Z-shaped) symmetry with a strike extent of approximately 95 km (Figures 3 and 4). Its eastern boundary is more ambiguous, although a series of WNW-ESE- to E-W-trending shears in the northeast and a decrease in magnetic and gravity intensities in the east are evident (Figures 3 and 4).

3.2.1. Lithological Domains

The identification and discretization of lithological domains broadly follows that of existing maps and previous interpretations, e.g., [46,68], including granite–gneiss basement with metasediments, quartzofeldspathic micaceous gneiss, magnetic I-type granites, gabbro-gabbrodiorite and meta-volcano-sedimentary units (Figure 3). Domains of (1) granite–gneiss basement with metasediments are defined by a low-to-medium magnetic intensity and relatively smooth magnetic textures; (2) quartzofeldspathic micaceous gneiss, including metasediments, calcsilicates and marble units, are defined by a low magnetic intensity and a relatively smooth magnetic texture; (3) magnetic I-type granites, including the Mesoproterozoic Balta Granite Suite and Engenina Adamellite, are defined by regionally high magnetic intensity with a stippled (high frequency) texture; (4) gabbro-gabbrodiorite units are defined by a very high magnetic intensity with high-frequency alternating magnetic highs and lows; and (5) a metasedimentary and metavolcanic host sequence, including metasiltstone, metasandstone, calc-silicate(s), marble, iron formation(s) and acidic, andesitic and basaltic volcanic successions, comprises a package of steepened or transposed, tectonically interleaved magnetic intensity lows and highs [68], which is particularly well-defined around the Prominent Hill area (Figure 3).

3.2.2. Structural Architecture

Whilst the structural architecture of the Mt. Woods Inlier presented herein differs somewhat from previous author's interpretations, e.g., [32,35,46,50,68], there are many overlapping similarities in the identification and characterization of key faults and shear zone networks. Internally, the Mt. Woods Inlier is dominated by NW-SE- and ENE-WSW- to E-W-trending major structures and domain/lithological contacts (Figures 3 and 4). The northern portion of the inlier consists of an acute wedge of tectonically interleaved stratigraphy, extending from the inlier-bounding Karari Shear Zone to the Cairn Shear Zone, dominated by ENE-WSW- to E-W-trending fabrics, contacts, faults, shears and shear zone networks (Figures 3 and 4).

The central and southern portions of the inlier consist of a sigmoidal block of tectonically interleaved lithologically variable domains constrained by the Cairn Shear Zone, Southern Overthrust, Bulgunnia Fault Zone and, tentatively, the Jupiter Shear Zone (see below), dominated by NNW-SSE- and WNW-ESE- to E-W-trending fabrics, contacts, faults, shears and shear zone networks (Figures 3 and 4). The re-interpretation of structures from the Mt. Woods Inlier delineates and describes the extent, geometry and interconnectivity of at least five well-developed, deep-seated shear zone networks and/or structural corridors: the Southern Overthrust, Panorama Shear Zone, Skylark Shear Zone, and Jupiter and Cairn Shear Zones/Corridors (Figures 3 and 4).

The Southern Overthrust, trending at approximately 335°, is defined by an 80 km linear zone of interconnected, anastomosing shears/faults (outlined in red, Figure 4), associated with an abrupt discontinuation of magnetic intensity, possibly representing a major north-dipping terrane-bounding thrust or thrust zone that extends to mid-crustal levels (>10 km), thereby signifying the SW margin of the Mt. Woods Inlier, e.g., [35,46,74].

The Cairn Shear Zone, trending at approximately 095°, is defined by a 120 km linear zone of interconnected, anastomosing shears/faults (outlined in blue in Figure 4) associated with the structural discontinuation of magnetic intensity along the northern margins of the Western and Central Geophysical Zones, defined by [46]. Outcrop studies by [46] and [32] reveal that the Cairn Shear Zone dips steeply to the north in the east and steeply to the south in the west, and is consistent with dextral, oblique-normal, north-side down kinematics.

The Panorama Shear Zone, trending at approximately 40°, is defined by a 30 km linear zone of abrupt discontinuation of magnetic intensity along the SE margin of a magnetic I-type (Balta Granite Suite)-dominated domain (outlined in bright green, Figure 4). Outcrop studies by [32,46] on the Moonlight Shear Zone suggest a synthetic splay of the Panorama Shear Zone, and infer that this is part of a Hiltaba-aged, steeply west-dipping structural network associated with sinistral, oblique-normal, west-side down kinematics.

The Skylark Shear Zone, trending at approximately 335°, is defined by a 60 km linear zone of interconnected anastomosing shears/faults (outlined in red on Figure 4) associated with the structural discontinuation of magnetic response and representing a major NW-SE-trending shear zone, interpreted by [32] as a basal detachment fault or fault zone. The interpretation presented here differs somewhat from [32] where, instead of a single fault or shear zone surrounding the "Central Geophysical Zone" [46], the Skylark Shear Zone consists of a series of NW-SE-trending components (outlined in red on Figure 4), possibly more consistent with the interpretation of [30]. The NNW-SSE-trending structure situated within the central parts of the "Central Geophysical Zone" is defined as a separate shear zone corridor, with respect to the Skylark Shear Zone, and is referred to as the Jupiter Shear Zone/Corridor (outlined in pink on Figure 4).

The Jupiter Shear Zone, trending at approximately 345°, is defined by a 22 km-long linear zone of interconnected and anastomosing shears/faults, collectively interpreted as a deep-seated, incipient shear zone. In principle, this shear zone network splays into the Carin Hill Shear Zone to the north and terminates against the concaved aeromagnetic low, which spatially overlaps with the NE-SW curvature of the Skylark Shear Zone interpreted by [32].

NW-SE-trending dykes of the Gairdner Dyke Swarm [75] occur within and around the inlier and are observed to intrude along pre-existing, NW-SE trending faults and shear zones in addition to cross-cutting most major structures and lithological/domain contacts.

3.2.3. Prominent Hill Area

A high concentration of IOCG-related occurrences, prospects and deposits is situated along the southern extents of the NW-SE-trending Southern Overthrust and Skylark Shear Zone corridors, particularly within the Prominent Hill area, at the interplay and obtuse intersection with the ENE-WSW-trending Bulgunnia Fault Zone (Figures 3 and 4).

This interaction manifests as a convex northeast shear and fabric inflection of the two NW-SE-trending deep-seated structures as they approach and intersect the ENE-WSW-trending Bulgunnia Fault Zone, within an area dominated by a combination of primarily ENE-WSW- and NW-SE-trending shears, fabrics and tectonostratigraphic contacts (Figures 3 and 4). The geometrical relationship between major structures within the Prominent Hill area (Figures 3 and 4) is similar, in many respects, to the Olympic Dam IOCG-deposit that occurs in proximity to NE-/ENE- and NNW-/NW-trending structures that intersect at obtuse angles, thereby constituting an overall stepped structural–geometrical relationship. This will be discussed in greater detail in a later section.

Unique to this part of the inlier is a large, rounded-cuspate, relatively competent gabbro-gabbrodiorite body immediately to the west of Prominent Hill and to the north of the Southern Overthrust (Figure 3). The gabbro-gabbrodiorite's rounded core and sheared or strung-out trailing edges, particularly on its eastern side, denote a large-scale rotated porphyroclast geometry: quartzofeldspathic micaceous gneiss and metacarbonates are entrained around its northern margin, while vertical to subvertical, tectonically interleaved lenses of metasiltstone, metasandstone, calc-silicate(s), marble, iron formation(s) and bi-modal volcanic successions, collectively referred to as host units or the host package, are entrained around its southern margin in the Prominent Hill mine area [68] (Figure 3). Interpretations from [68,70,76,77] suggest that the relatively competent gabbro-gabbrodiorite intrusion was flanked by strain shadows, during NE-SW-directed compression during D_1, and subsequently displaced and sheared into the dominant fabric.

From a finite element analysis perspective, the zone around Prominent Hill constitutes a series of thin, steeply dipping, tectonically interleaved units with a structural complexity derived from the cumulative southward-verging thrusting and transposition to steeper dips, and subsequent strike-slip (oblique?) deformation and rotation around the gabbro-

gabbrodiorite body. A variety of lithologies, with differing competencies, have therefore undergone an extensive and relatively high-strain history, resulting in a zone of interleaved, mixed, vertical to subvertical units, adjacent to a very competent body or "stress-riser" (Figures 3 and 4).

4. Structural Preparation and Deformation Related to Hydrothermal Mineralisation

In this contribution, the Mt. Woods Inlier is considered to have undergone (protracted) progressive near- to far-field regional stress regimes from the Kimban Orogeny (1740–1690 Ma), Kararan Orogeny (1610/1575–1540/1530 Ma) and the overlapping Olarian Orogeny (approx. 1600–1500 Ma), onwards, e.g., [29,30,32,38–41,46]. Based on the overall maximum stress orientations from these orogenic episodes, we summarize two distinct stress regimes (D_{n+1} and D_{n+2}) that are particularly important for the structural preparation and deformation—prior to and during—the geologically brief NNW-SSE-oriented extensional event (1595 Ma to 1590 Ma) co-incident with IOCG hydrothermal fluid flow and mineralisation (Figure 5A,B). In this context, "structural preparation" refers to the establishment of the structural framework that was subjected to the subsequent, short-lived extensional event that accompanied mineralisation.

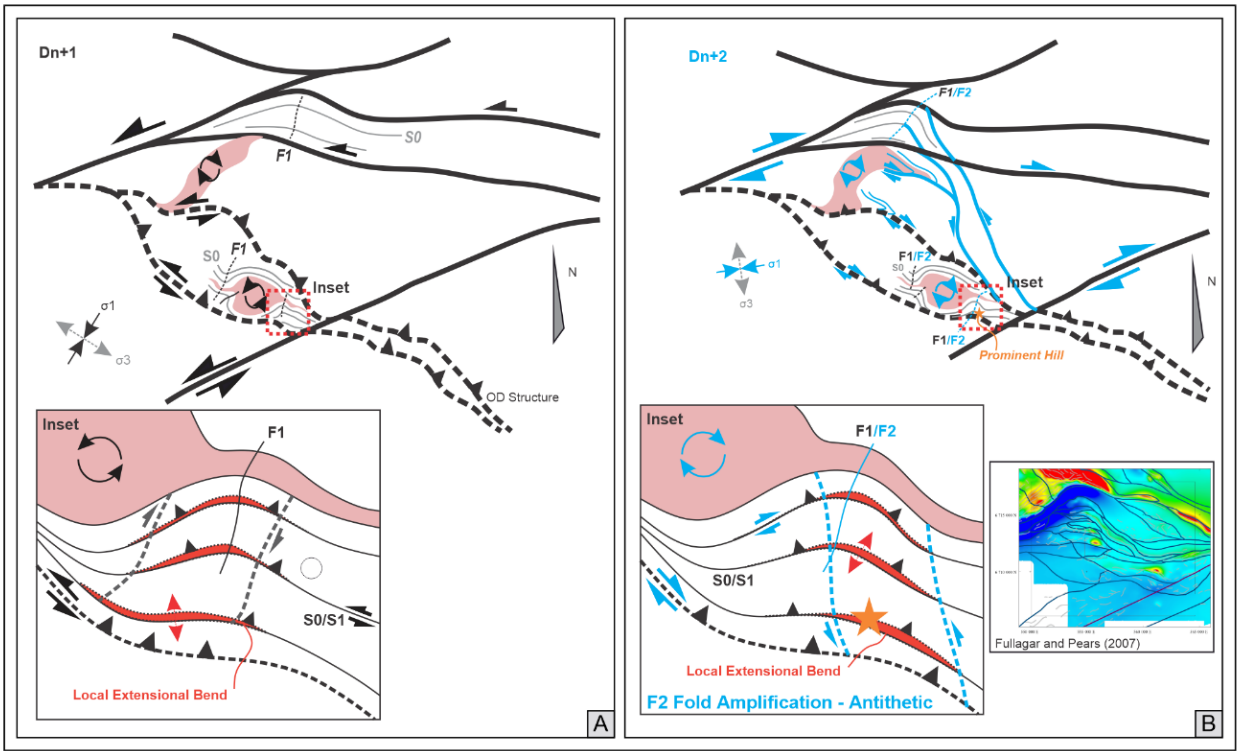

Figure 5. Schematic summary of key structural events, colloquially termed D_1 and D_2. (**A**) Pre- to Syn-Kimban and Early Kararan Orogeny (~1780–1670 Ma). Key features include left-lateral shearing along the Karari and Bulgunnia Shear/Fault Zones and internal WNW- to E-W-trending synthetic shear zone, development of zones of fabric inflection, anticlockwise rotation of the gabbro/gabbrodiorite body and "stringing" of its tails or terminations into the surrounding fabric and structures. (**B**) Late Kararan and Olarian Orogeny (~1600–1500 Ma, [46])—IOCG mineralisation (1595–1585 Ma, [30]). Key features are a reversal in stresses (E-W compression, N-S extension), intrusion of the Hiltaba Suite throughout the region, the development of an incipient shear zone and dilation of many of the pre-existing structures and fabrics. This dilation was particularly well-developed in the Prominent Hill area, wherein local extensional bends accommodated Fe-rich hydrothermal fluids and mineralisation, expressed by several TMI anomalies in the study of [64], shown as an inset in (**B**).

D_{n+1}, interpreted to coincide with the Kimban Orogeny (1740–1690 Ma) (Figure 5A), is characterized by initial NE-SW-directed shortening, dominated by south-westward verging thrusting, and a sinistral or left-lateral sense of movement that was largely related to the oblique convergence and lateral escape on the northern margin of the Gawler Craton. The ENE-trending Bulgunnia and Karari Fault/Shear Zones, and associated relay or synthetic shears, are interpreted to be associated with the transposition and reactivation of pre-existing, NW- to NNW-trending Kimban rift structures (e.g., Southern Overthrust, Skylark Shear Zone and/or Olympic Dam-trending structures, including the Fitzgerald Shear and Elizabeth Creek Faults) and the anticlockwise rotation of the gabbro-gabbrodiorite intrusion to the NW of Prominent Hill (Figure 5A). This framework coincides or overlaps with the development of fabrics (S_1/S_2) and structures (F_1/F_2) during the deformation phases of D_1 and D_2 of [35,46], attributed to early and late stages of the Kimban Orogeny, respectively.

The early stages of the Kararan Orogeny are marked by a shift in the principal stress axis, generating NNW-SSE-orientated compression (1630–1595 Ma), followed by the geologically brief NNW-SSE-oriented extensional event (1595 Ma to 1590 Ma), in turn followed by the continued NNW-SSE-oriented compression (1585–1550 Ma) (after [30,31]. D_{n+2} is interpreted to coincide with the onset of the brief NNW-SSE-oriented extensional event (Figure 5B), and is characterized by kinematic reversal along many structures, including the Southern Overthrust, Karari, Bulgunnia and Skylark Fault/Shear Zones, to dextral or right-lateral senses of movement, in turn due to the rotation of the maximum stress axis to a broadly NNW-SSE orientation during 1630–1595 Ma. The stress-state switch from NNW-SSE-oriented compression to NNW-SSE-oriented extension (1595 Ma to 1590 Ma) acted on the pre-existing structural geometries established in D_{n+1} and was synchronous with the emplacement of the Balta Granite Suite (~1584 $\pm$ 18 Ma), the Gawler Range Volcanics (~1592 $\pm$ 3 Ma) and IOCG-related mineralisation.

5. IOCG Deposit Structural Architecture

There are several IOCG-type deposits within the Gawler Craton and Cloncurry District of Australia (e.g., Olympic Dam, Prominent Hill, Ernest Henry), the Carajás Region of Brazil (e.g., Sossego, Salobo, Cristalino) and the Coastal Cordillera of the Andes in Chile (e.g., Candelaria) [78] (Figure 6). IOCG-type mineralisation at Prominent Hill is a prime example of the hematite-rich endmember of the IOCG deposit model type [57,79,80]. It consists of polymetallic haematitic breccia complexes, dominated by chalcocite–bornite–chalcopyrite assemblages, hosted in a package of volcano-sedimentary and carbonate units, e.g., [57,81]. The Cu-Au-rich, hematite-bearing to hematite-rich breccias were formed by numerous phases of hydrothermal brecciation, pervasive replacement and cataclastic milling, resulting in significant multi-stage alteration assemblages and polymetallic (Fe, Cu, Au, Ba, F, U, Ce and La) enrichment and mineralisation, e.g., [26–28]. The altered, brecciated and mineralised volcano-sedimentary units at Mt Woods are hosted at the obtuse intersection between an ENE-trending gravity anomaly, NW- to NNW-trending structures and magnetic anomalies. Significantly, geopetal markers demonstrate that economic mineralisation occurred after the tilting of the host rocks into their present, steep to near-vertical orientations, e.g., [26,27]. Similar to Prominent Hill in many respects, the Olympic Dam IOCG deposit partly occupies both NE-/ENE- and NNW-/NW-trending structures that intersect at obtuse angles, exhibiting an overall stepped structural–geometrical relationship, e.g., [30] (Figure 6).

The geometry of the Sossego IOCG deposit and its controlling structures suggest a similar geometry, in the form of an obtuse angle between the Pista and Sequerinho orebodies, in turn following steeply dipping WNW- and ENE-trending structures (Figure 6) [82]. This relationship between major structures or contacts, fluid flow, brecciation and concomitant space and permeability creation, and IOCG-type mineralisation are also prevalent in the Salobo, Cristalino and Candelaria IOCG deposits (Figure 6). Throughout the abovementioned IOCG deposits, orebody morphologies are typically described as steeply plunging to subvertical breccias and/or stockworks with sharp boundaries that exhibit overall pipe-like or columnar geometries, commonly described as chimneys or apophyses, e.g., [30,83,84]. These are situated at the obtuse intersection of structures and/or contacts and may have been created from a myriad of intersecting conjugate extensional fractures, thereby creating a zone of structural permeability. Throughout the Olympic Dam IOCG Province, the intersection between (N)NW-trending and (E)NE-trending major structures is therefore considered to be a high- or first-order control of fluid movement, e.g., [30]. In other words, IOCG mineralisation is preferentially localized along steeply plunging, effectively prolate, conjugate intersections that serve as crustal-scale fluid conduits that are conducive to increased permeability and throughput of hydrothermal fluids and the resultant mineralisation, e.g., [30].

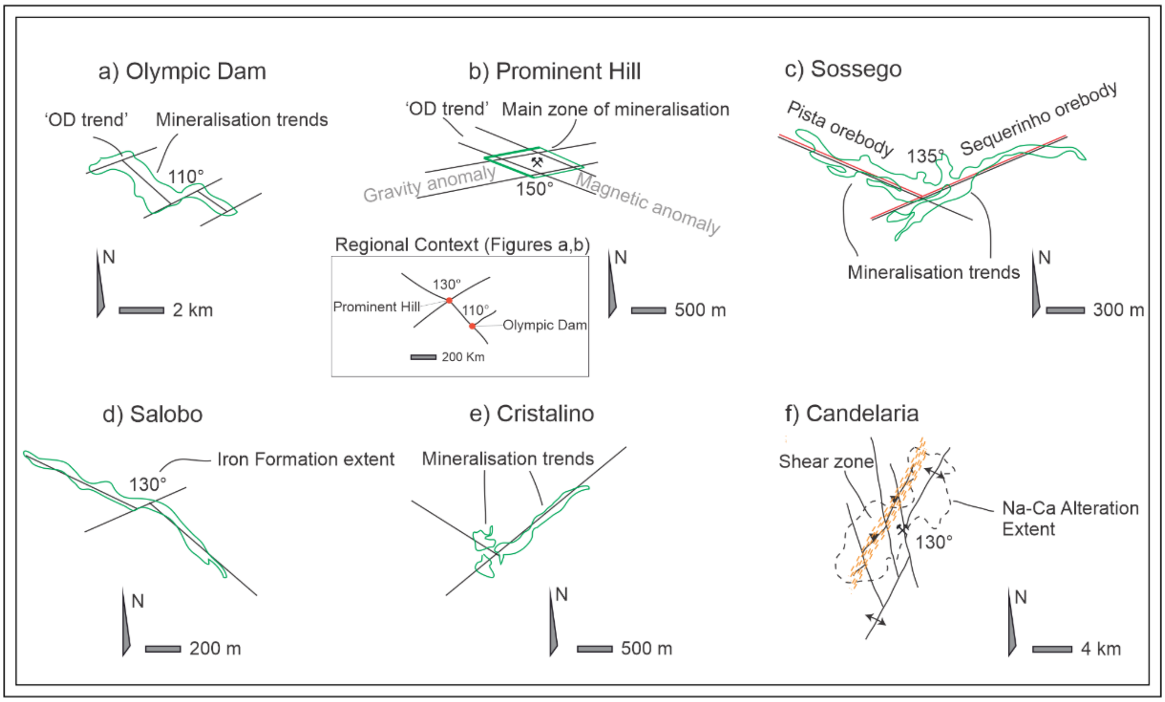

Figure 6. Geometries and mineralisation trends of IOCG mineralisation at Olympic Dam, Prominent Hill, Sossego (Pista and Sequerinho orebodies), Salobo, Cristalino and Candelaria. These examples highlight the relationships of mineralisation with the conjugate extension of two or more major structures or fabrics, at obtuse angles to one another, resulting in a "stepped" pattern of mineralised zones, space creation, dilational breccias and the formation of brecciated, permeable pipe-conduits at their intersections.

6. Stress Mapping

Stress mapping is a numerical modelling technique that translates solid geological features into a proxy map of material or rock engineering parameters, in order to simulate the distribution and relative magnitudes of stress and strain within a geological terrane during a deformation event, e.g., [85]. There are two main approaches: discrete element analysis (DEA), after [86], and finite element analysis (FEA), e.g., [87,88]. The latter is more amenable to addressing natural systems, can accommodate discontinuous or 'blind' faults and shears, and is capable of dealing with complex geometries and loading conditions.

The application of FEA to hydrothermal systems relies on the principle that structural–geometrical elements govern pathways and fluid pressure gradient-driven hydrothermal fluid flow, and that hydrothermal mineral deposits are primarily controlled by deformation-enhanced fluid flow and flux along dilational structures and/or sites of increased permeability [5,25,89–92]. This has previously been used to simulate deformation-induced fluid flow within epigenetic, polymetallic Pb-Zn-Ag-Au and orogenic (Au) hydrothermal mineral deposits, e.g., [85,93–97].

Stress mapping, either finite element or discrete element, requires several key parameters in order to model the stress or strain variations within structurally complex geological media. These parameters include (after [85]): (1) orientations and approximate magnitudes of far-field horizontal stresses during a well-constrained temporal window of hydrothermal activity; (2) an understanding of the structural–geometrical controls on fluid movement and the mode of mineralisation; (3) high-resolution geological input features, such as a GIS-based interpretation of available geophysical or remote sensing data; (4) near-verticality of key structures or contacts; and (5) no significant post-mineralisation deformation. These conditions and parameters are met for the study area that incorporates the Mt Woods Inlier. To model the stress (and resultant strain) distribution, the input model translates the relative variation in rock strengths, rheologies, material properties (Table 1), their structural–geometrical configuration and generalized contact/shear conditions (from the re-interpreted structural and geological map (Figure 3) into to a proxy map of parameters and materials that may be subjected to simulated stress conditions. The FEM software package, Phase2 9.0, developed by Rocscience, was used to simulate the induced stress and strain distributions during the key deformation event.

Table 1. FEA input material properties.

Material	Failure Criterion	Tensile Strength (MPa)	Friction Angle°	Cohesion (MPa)	Young's Modulus (MPa)	Poisson's Ratio	Unit Weight (Mn/m^3)
Gabbro-gabbrodiorite	Mohr–Coulomb	23	42	28	73,000	0.22	0.030
Magnetic I-Type Granite	Mohr–Coulomb	15	36	20	55,000	0.23	0.0255
Granite–Gneiss and Metasediments	Mohr–Coulomb	15	36	20	54,000	0.21	0.025
Quartzofeldspathic-Micaceous Gneiss	Mohr–Coulomb	18	34	20	46,000	0.18	0.025
Host Sequence (MM)	Mohr–Coulomb	15	36	20	54,000	0.23	0.026
Host Sequence (LM)	Mohr–Coulomb	20	30	22	39,000	0.16	0.024

6.1. Finite Element Analysis—Model Parameters

The following parameters and conditions were established for finite element analysis (after [85]): (1) estimates of the orientations and magnitudes of the far-field, horizontal stresses (NNW-SSE directed extension) acting on the Mt. Woods Inlier during the well-constrained, geologically short (1595–1590 Ma) interval of IOCG-related hydrothermal fluid flow and mineralisation (Figure 6), e.g., [30,31]; (2) structural–geometrical controls and mode of IOCG-type mineralisation within the Olympic Dam Province, using Prominent Hill and Olympic Dam as proxies, whereby these occur along steeply dipping, ENE- and NNW-trending structures, fabrics or contacts and particularly at their intersections (Figures 3, 4 and 6), e.g., [30]; (3) near-verticality of most or all structural features throughout the Olympic Dam IOCG Province, including the Mt. Woods Inlier [98]; (4) no significant post-mineralisation deformation; (5) an inferred Mohr–Coulomb elasto-plastic behaviour during deformation, e.g., [99,100]; and (6) as no specific information is readily available for these parameters, lithologies, structures and fabrics have been assigned reasonable failure criterion, uniform slip criterion, tensile strength, peak cohesion, peak friction angle, Young's Modulus' and Poisson's ratios (Table 1) based on values obtained from the literature.

The model is relatively robust and is not sensitive to minor variations in these latter parameters. Interpreted domains of magnetic I-type granite, granite–gneiss and metasediments and quartzofeldspathic-micaceous gneiss are assigned very similar material/strength parameters, while gabbro-gabbrodiorite is appropriately assigned parameters that render it more competent, such as a higher tensile strength and higher Young's Modulus (Table 1). The mineralised package to the S and SE of the gabbro-gabbrodiorite body (Figures 3 and 4) has been subdivided, based on its magnetic signature, into components that are either metasedimentary or meta-volcanic (low magnetic signature to moderate magnetic signature, respectively) and accordingly attributed with a bimodal set of reasonable strength parameters, to represent a narrow zone of interleaved, mixed, vertical to subvertical units.

The numerical model is deformed under biaxial compression conditions with horizontal σ_2 and σ_3 during the simulated, mineralisation-related D_{n+2} extensional event

(Figure 5B). To avoid edge effects during FEA loading simulations, a buffer of 40.3 km was added onto the northern and southern margins of the model, while a buffer of 24.7 km was added to the E and W margins of the model (Figure 7). In order to avoid excessive movement of the dense array of shears within the northern parts of the area of interest, only the southern margin of the model was extended in an SSE direction, while the top of the model was anchored (Figure 7) resulting in SSE movement vectors at each model node. The eastern and western margins of the model are unrestricted to thereby transmit the E-W/ENE-SSW compression from intermediate principal stress (σ_2) during D_{n+2}.

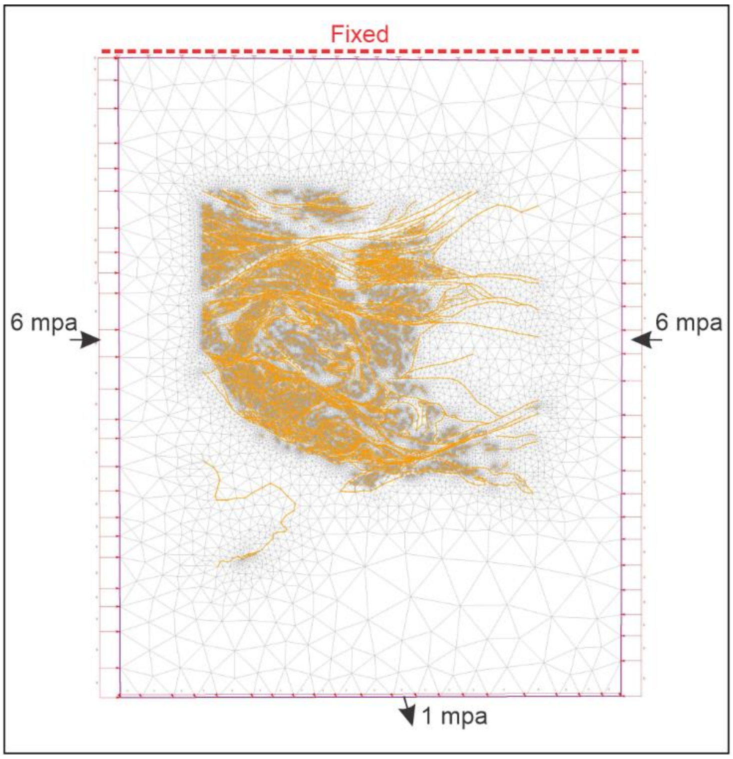

Figure 7. Schematic FEA framework of loading conditions for the simulated stress regime.

6.2. Finite Element Analysis—Simulation Outputs

FEA outputs, including differential stress and shear strain heat maps, effectively illustrate the lateral variations and distribution of stress and strain across the lithologically variable and geometrically complex Mt. Woods Inlier (Figures 8–10), during the simulated D_{n+2} deformation event, co-incident with IOCG-related hydrothermal activity.

Differential stress is defined as $\Delta\sigma = (\sigma_1 - \sigma_3)$, where σ_1 and σ_3 are the maximum and minimum principal stresses. This quantifies the relative magnitudes and distribution of stress states throughout the geological media. The heterogeneous distribution of differential stress (Figure 8) is broadly comparable to the underlying lithological units across the modelled terrane, wherein concentrations of particularly high differential stress occupy regions of rheologically competent lithological domains, such as magnetic I-type granite, whilst differential stress maxima occur along the margins of the relatively more competent gabbro-gabbrodiorite body to the NW of Prominent Hill (Figures 3 and 8).

NNW-SSE to N-S corridors of relatively low and or laterally variable differential stress are observed throughout the inlier. The most definitive of these is within the Prominent Hill region, wherein a 10 km-wide low-differential-stress corridor extends from the Bulgunnia Fault Zone into the Jupiter Shear Zone (Figure 8). These corridors, although more subdued, also occur on the western flanks of the gabbro-gabbrodiorite body, and within the northern remnants or extensions of the Jupiter Shear Zone (Figure 8). Spatial heterogeneity in differential stress across the Mt. Woods Inlier (Figure 8) were represented using the Terrain Ruggedness Index (TRI) developed by [101] (Figure 9). There is an obvious spatial correlation between zones or corridors of rapid lateral changes or heterogeneity in differential stress (Figures 8 and 9) and known occurrences, prospects and deposits that show hydrothermal mineralisation, including Prominent Hill, Blue Duck A, Prominent Hill West, Proteus, Neptune Triton, Taurus, Bellatrix, Joes Dam, Manxman A2, Manxman A4, Manxman B, Jupiter and Halifax Hill. This suggests a unifying control, related to rapid changes or lateral gradients in differential stress (Figure 9), on induced hydrothermal fluid flow. The high-gradient, along-strike lateral variations in differential stress are interpreted as zones or corridors prone to mechanical failure and space creation, in turn susceptible to localized throughput of contemporaneous IOCG-related hydrothermal fluids.

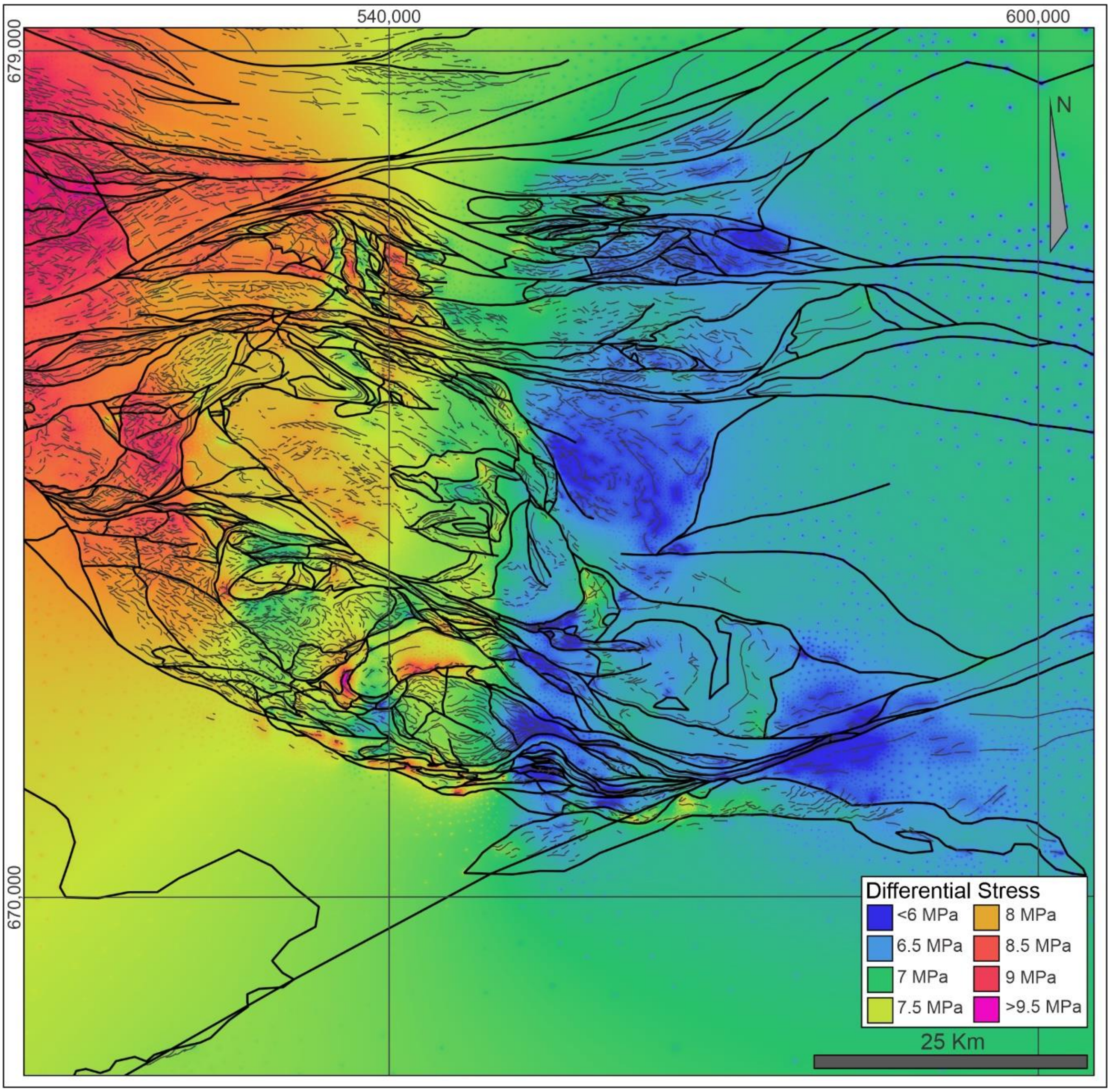

Figure 8. Map illustrating the distribution of differential stress throughout the Mt. Woods Inlier during the simulated stress regime.

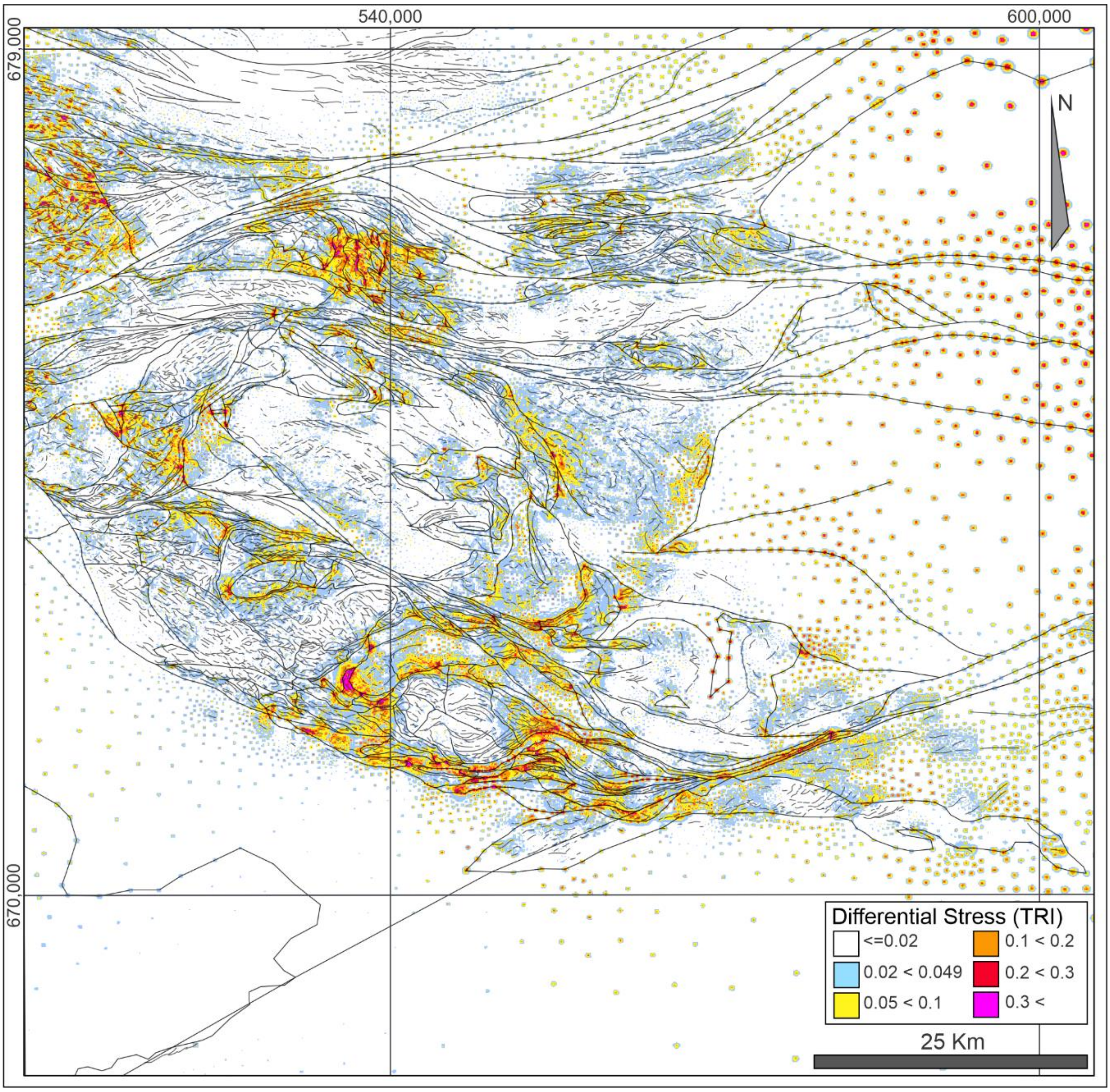

Figure 9. Differential stress, shown as a Terrain Ruggedness Index (TRI) map, showing spatial heterogeneity across the Mt. Woods Inlier. Warmer colours indicate high changes in differential stress while cooler colours indicate lower changes in differential stress. Areas of particularly high differential stress occur around the large gabbro-gabbrodiorite body in the southern extent of the Mt. Woods Inlier, with another notable zone to the north of the Cairn Hill Shear Zone.

Shear strain, defined as $\varepsilon_{xy} = \frac{1}{2}\left(\frac{\partial v}{\partial x} + \frac{\partial u}{\partial y}\right)$, quantifies the average change in the angle between elements during simulated deformation (Figure 10). The heterogeneous distribution of shear strain represents structurally variable loci across the modelled terrane, wherein concentrations of particularly high shear strain occupy regions of favourably orientated, interleaved tectonostratigraphy (Figure 10). These shear strain loci or concentrations developed as a function of strain incompatibility [90], triggered by enhanced geometrical–structural interconnectivity of structures, fabrics, contacts and rheologically variable lithological packages (Figures 3 and 10). A qualitative spatial correlation, between areas of enhanced shear strain concentrations (Figure 10) and known occurrences, prospects and deposits of hydrothermal mineralisation, is evident, most notably the Prominent Hill IOCG deposit and the Peculiar Knob Fe-occurrence on the SE and NW flanks of the gabbro-gabbrodiorite body, respectively.

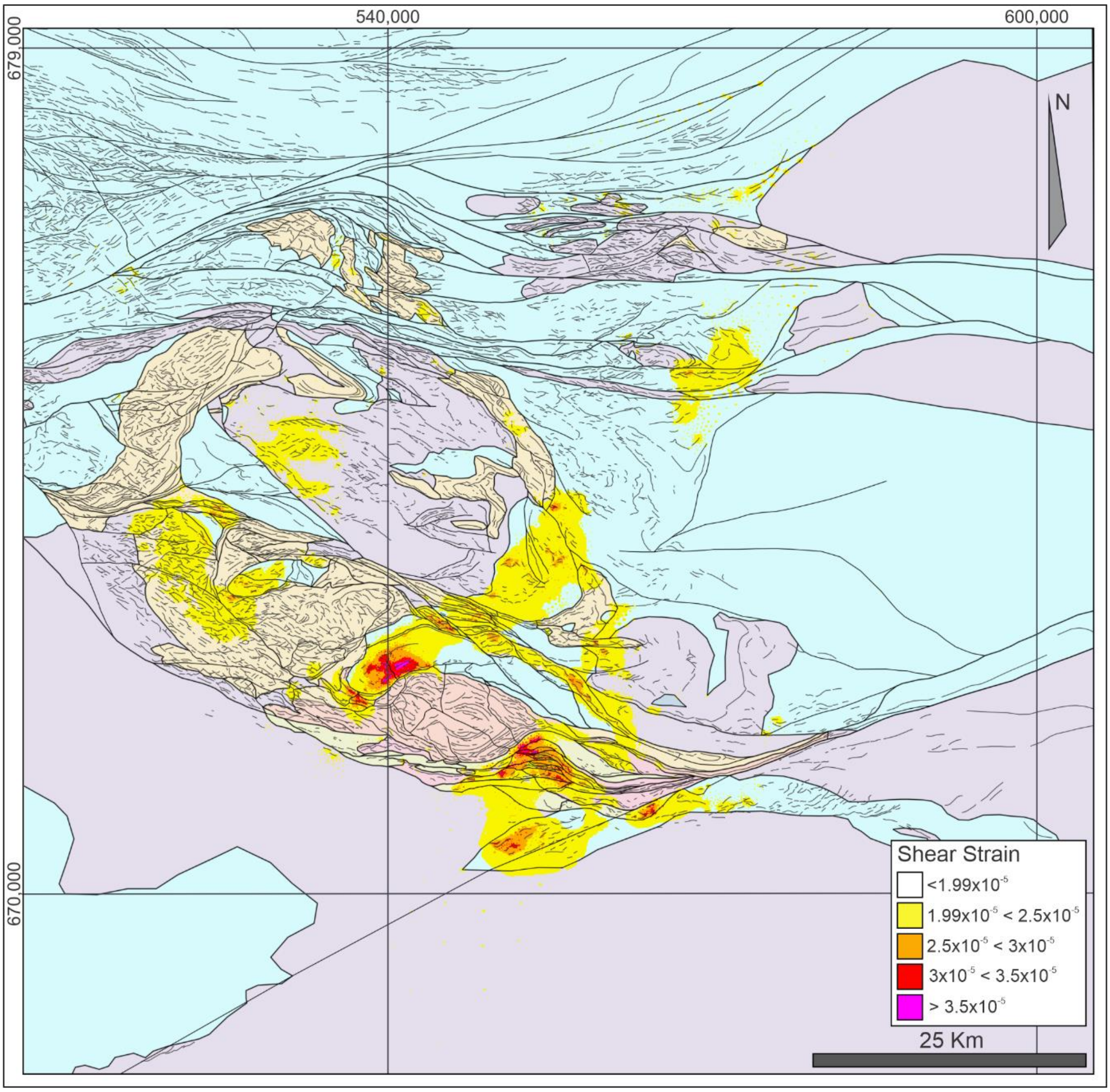

Figure 10. Shear strain superimposed on the structural–lithological interpretation. Areas of particularly high shear strain occupy regions of favourably orientated and interleaved tectonostratigraphy in proximity to—and adjacent to—the large gabbro-gabbrodiorite body in the southern extent of the Mt. Woods Inlier.

7. Targeting

The abovementioned parameters and observations outlined in the FEA may be combined with additional, more conventional targeting GIS layers (Figure 11), to generate a target index (Figure 12). Essential conditions for mineralisation are permeability pathways in the Earth's crust and/or mantle and long-lived or multiple stages of brecciation, dilation and auto-brecciation during a transient mobilization event [31,102]. This follows the approach of defining conduits, types of structural trap-sites, and to a lesser degree, hosts, seals and plumbing fluid systems (after [14]). Key or specific requirements in the Gawler Craton (after [103]) include: position within the Olympic Dam corridor; a host rock association with the Hiltaba Granite Suite, including the Balta Granite Suite and Gawler

Range Volcanics; polymetallic (Cu-Ag-Co-Pb-Zn) mineralisation that overlaps with the Olympic Dam age of 1590 Ma; mineralisation loci in proximity to major structures; and an association with strong gravity and magnetic signatures and IOCG alteration. Locally, this includes the alignment along ENE- and NNW-trending structures (or foliations/fabrics), in the hanging wall of ENE-trending structures, and/or at the confluence/intersection of ENE- and NW-trending structures [30].

The general guidelines outlined in [2,104] were followed in the development of a Target Index for IOGC Prospectivity. Initial emphasis was given to the identification of deep, trans-lithospheric mineralizing structures (after [104]), followed by the establishment of critical components of the mineralisation process and the means by which these could be extracted from the spatial datasets (after [2]) in this case, primarily aeromagnetic data (Figure 2). These were, collectively, combined with the stress–strain maps.

Based on the maturity of the area, and considering the data coverage and types, the Venn diagram approach (after [2]) was applied, wherein targets are proposed based on a conjunction or overlap of several parameters (Figure 11). Targeting also addresses and weighs parameters by way of a hierarchy of controls (Figure 11). Target rankings were compiled according to [2] by assigning scores to each essential, ranked parameter and then summing these scores to provide a total target score, which was then plotted and compared to mineralisation loci (Figure 12). Due to the presence of several world-class deposits in the vicinity, we reasonably assume that a fluid source is present:

1. Within zones that exhibit rapid lateral changes or heterogeneity in differential stress, for instance along the strike of host lithologies around Prominent Hill, comprising approximately 1.5 km-wide N-S-trending corridors (Figure 8) (Plumbing Fluid System: Focused Fluid Flow in Relatively High-Strain Shear Zones). In terms of scoring this was treated as a binary (Table 2), whereby areas that exhibit rapid lateral changes or heterogeneity in differential stress >0.05 in the TRI (Figure 8) are considered important in weighting or scoring (Figure 11A);
2. High-shear strain zones occupy regions of favourably orientated interleaved tectonostratigraphy susceptible to concentrated strain incompatibilities (Depositional Site: Structural Trap) (Figure 11B). Gradational distributions were binned into categories and weighted accordingly (Table 2);
3. Proximity to major ENE-trending shear zones (Plumbing Fluid System: Deep Fluid Conduit: Crustal-Scale Shear Zone). Known or established polymetallic mineralisation occurs within a distance of approximately 12–16 km north of the Bulgunnia Fault Zone, along the Olympic Dam-trending structure. However, Prominent Hill is 6 km from the Bulgunnia Fault Zone, while Cairn Hill is 7 km from the Karari Shear Zone (Figures 1 and 2). A multi-buffer of 10,500 m, 3240 m and 1800 m was selected for the Bulgunnia and Karari Fault/Shear Zones (Figure 11C). Consequently, a lower weighting was assigned to the 10,500 m buffer zone on either side of these shear zones, while buffer zones 3240 m and 1800 m attracted higher relative weightings or scores (Table 2);
4. Proximity to the Olympic Dam-trending structures (Plumbing Fluid System: Deep Fluid Conduit: Crustal-Scale Shear Zone). Prominent Hill is situated between two deep-seated, NW-trending shear zone corridors, including the Southern Overthrust and Skylark Shear Zone (Figure 2), which are interpreted as extensions of the Elizabeth Creek Fault Zone. A buffer of 2000 m was selected for each shear, comprising multiple shears within a total width of up to 7.5 km (Figure 11D). In terms of scoring, this was treated as a binary (inside vs. outside) (Table 2);
5. Within the host package or host units, also treated as a binary (inside vs. outside) (Trap: Chemical Trap) (Figure 11E). However, so as not to negatively bias areas outside of the Prominent Hill area, due to the fact that host units are restricted in their extent, this only attracts a relatively low score overall (Table 2);
6. Contacts that comprise significantly contrasting competencies/rheologies, for example between the components of the host package around Prominent Hill and at the contact

of the gabbro-gabbrodiorite body, as these have undergone dilation and extension (Depositional Site: Rheological Trap: High Rheological Contrast) (Figure 11F). A narrow or conservative buffer of 200 m was applied for these in terms of scoring. This was treated as a binary (Table 2) (inside vs. outside);

7. Intersection points between pairs of structures that display an obtuse intersection angle (Figures 4 and 11G) (Plumbing Fluid System: High-Damage Zones at Fault Intersections). These were manually identified in ArcView, and were selected where the NNW-SSE trend (direction of D_{n+2} extension) bisected or approximately bisected a mutually obtuse angle. Buffers of 100 m, 250 m, 500 m and <1000 were applied and appropriately scored (Table 2).

Table 2. IOCG targeting index inputs and their relative weights.

	Input Layer	Unit (Distance (m), Radians, etc.)	Assigned Individual Points/Weights
1	Differential Stress	$X \geq 0.05$	100
		$X < 0.05$	0
2	Shear Strain	$X \geq 0.000035$	100
		$0.000035 < X \leq 0.00003$	75
		$0.00003 < X \leq 0.000025$	50
		$0.000025 < X \leq 0.00002$	25
		$X < 0.00002$	0
3	Proximity to ENE-Trending Structures	≤ 1800	100
		≤ 3240	60
		$\leq 10{,}500$	10
		$>10{,}500$	0
4	Proximity to Olympic Dam-Trending Structures	$X \leq 2000$	100
		$X > 2000$	0
5	Host Package	IN	100
		OUT	0
6	Competency Contrast	$X \leq 200$	100
		$X > 200$	0
7	Obtuse Intersection	$X \leq 100$	100
		$100 < X \leq 250$	75
		$250 < X \leq 500$	50
		$500 < X \leq 1000$	25
		$X > 1000$	0

The results of a GIS-based combination of each weighted spatial layer (Table 2) produces a semi-quantitative target index (Figure 12) detailing the relative IOCG prospectivity within the Mt. Woods Inlier. The target index independently identifies known occurrences, prospects and deposits of IOCG-related hydrothermal mineralisation within the Mt. Woods Inlier including: Prominent Hill, Prominent Hill West, Blue Duck, Neptune, Proteus, Triton and Larissa. (Figure 12B). In addition, it highlights other areas that show the same or a very similar confluence of features and their resultant scores, thereby comprising areas of interest for further exploration. It should be noted that the target index "heat map" should be used as another layer in any regional exploration effort, in conjunction with more detailed or higher-resolution geophysical data and soil-sampling programs.

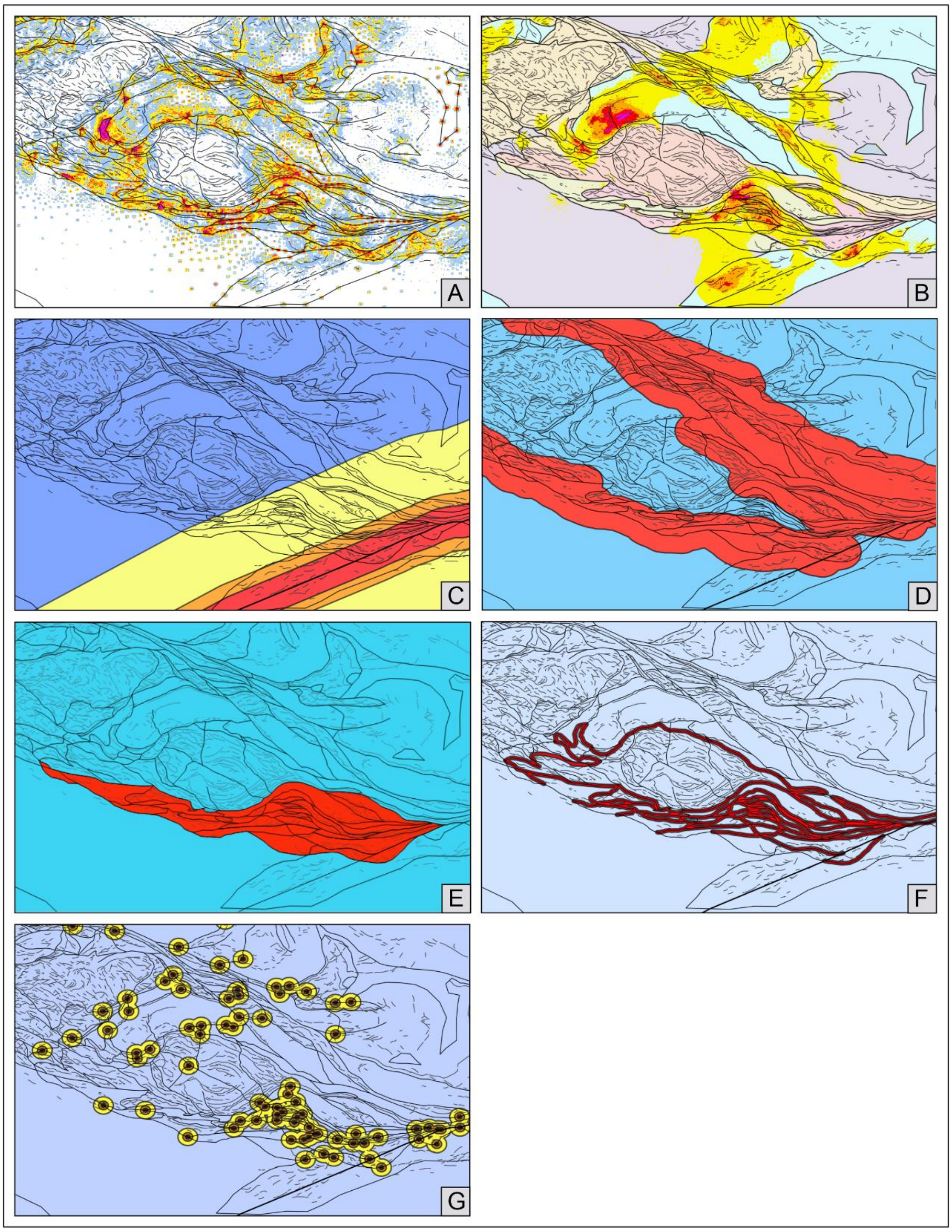

Figure 11. Input layers for the target index: (**A**) spatial changes in differential stress during the simulated stress regime; (**B**) high concentrations of shear strain during the simulated stress regime; (**C**) three buffer zones with weighting according to their proximity to the major ENE-trending Karari and Bulgunnia Shear/Fault Zones; (**D**) a buffer surrounding the interpreted Skylark Shear Zone and Southern Overthrust that represent probable extensions of Olympic Dam-trending deep-seated 1st-order structures (viz., the displaced Elizabeth Creek Fault Zone trend); (**E**) tectonostratigraphic host package of IOCG mineralisation in the Prominent Hill area; (**F**) contacts between significantly contrasting rock competencies, for example between the components of the host units around the Prominent Hill deposit and at the contact of the gabbro/gabbrodiorite body with surrounding tectonostratigraphy; and (**G**) Point/Ring buffers surrounding the obtuse intersection angle between structures, foliations or structure–foliation interactions (as per Figure 6).

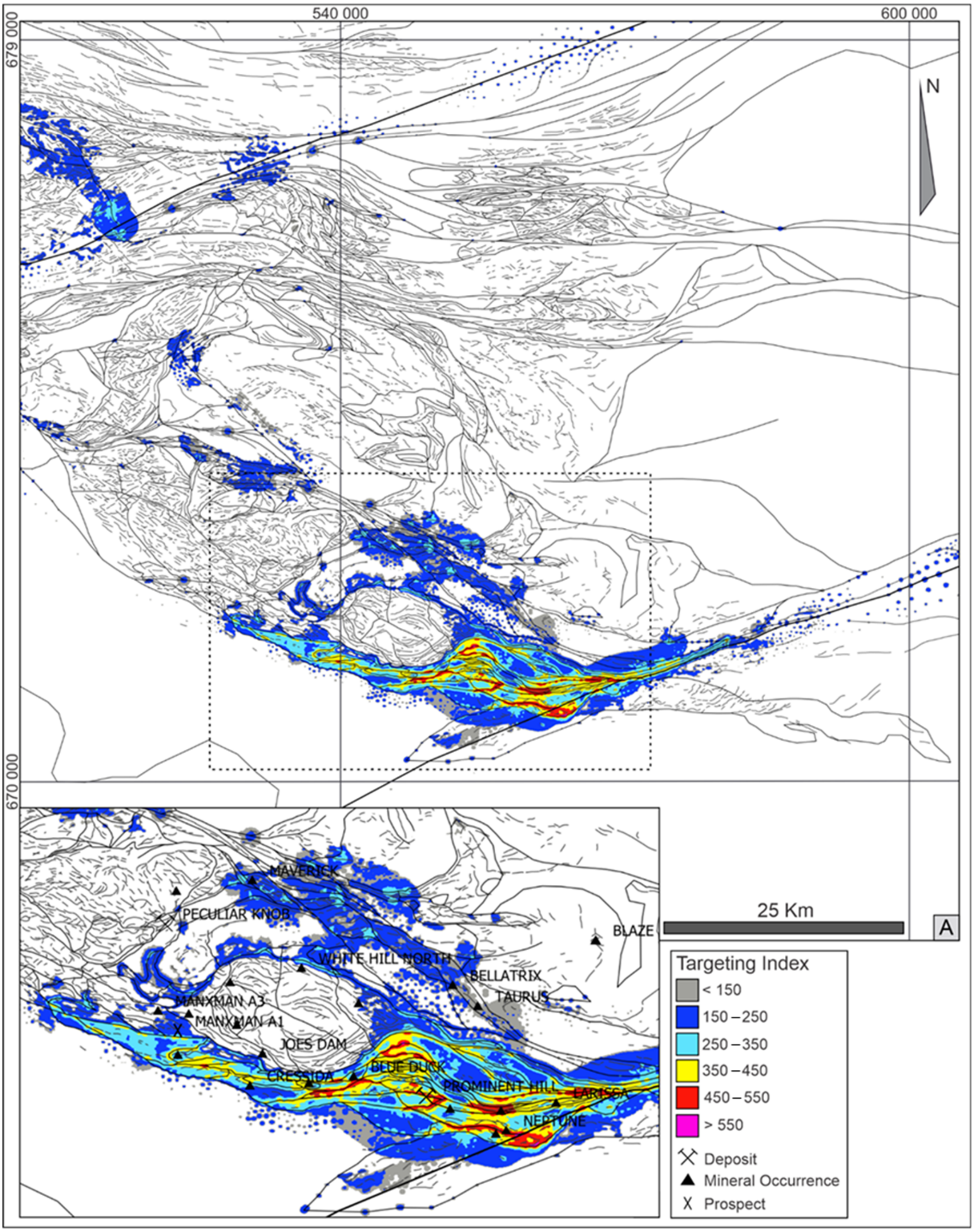

Figure 12. Integrated target index or heat map of IOCG prospectivity across: (**A**) the Mt. Woods Inlier and (**B**) across the Prominent Hill region (inset). Areas of high IOCG prospectivity (warmer colours) coincide with known IOCG-related occurrences, prospects and deposits and include: Prominent Hill, Prominent Hill West, Blue Duck, Neptune, Proteus, Triton and Larissa.

8. Conclusions

This study describes an integrated approach to mineral systems target generation for IOCG prospectivity for the Mt. Woods Inlier, Gawler Craton, South Australia, through the combination of structural–geometrical controls on IOCG-related hydrothermal mineralisation. Common features of global analogues, the re-interpreted structural architecture of the Mt. Woods Inlier and the simulated stress-state conditions during the proposed brief NNW-SSE extensional event between 1595 Ma to 1590 Ma, coincident with IOCG-related hydrothermal activity, were worked into the targeting methodology. The following observations and results are noteworthy:

The re-interpretation of structures from the Mt. Woods Inlier outlines and describes the extent, geometry, interconnectivity and role of five well-developed, deep-seated shear zone networks and/or structural corridors, including the Southern Overthrust, Panorama Shear Zone, Skylark Shear Zone, and the Jupiter and Cairn Shear Zone Corridors;

Globally, IOCG deposit orebody morphologies typically consist of steeply plunging to subvertical breccias and/or stockworks that exhibit overall pipe-like or columnar geometries. These appear to be situated at the obtuse intersections of structures and/or contacts. Throughout the Olympic Dam IOCG Province, the intersection between (N)NW-trending and (E)NE-trending major structures re-emerges as a recurring theme, both at the local scale and at a regional scale;

The Prominent Hill area is dominated by a combination of primarily ENE-WSW- and NW-SE-trending shears, fabrics and tectonostratigraphic contacts. It exhibits the interplay of obtuse intersections of the ENE-WSW-trending Bulgunnia Fault Zone, and NW-SE-trending Southern Overthrust and Skylark Shear Zone;

Unique to this part of the inlier is a large, rounded-cuspate competent gabbro-gabbrodiorite body that occurs immediately to the northwest of Prominent Hill. This is considered to be instrumental in mineralisation, by playing a significant role in establishing the pre-mineralisation structural geometry and by constituting an extraordinary rheological stress-riser during the subsequent mineralisation-related deformation;

Finite element analysis simulates a brief period of terrane-scale deformation, producing relative stress and strain distribution maps throughout the Mt. Woods Inlier. Known occurrences of IOCG-related mineralisation loci spatially coincide with rapid lateral changes in differential stress and regions of high shear strain. The patterns inherent in these maps, on their own, suggest that this is a profitable line of research for simulating deformation coincident with IOCG-related hydrothermal activity within the Inlier and in similar terranes;

The results are independent of, or rather do not rely on, the positions of known occurrences, prospects and deposits;

The resultant target index, which incorporates the various layers produced for this study, shows a strong correlation with known occurrences, prospects and deposits;

This technique is uniquely suited for exploration under deep cover, as is the case across much of the study area.

Author Contributions: Conceptualization, J.N.G.-J., I.J.B. and B.S.; Data curation, J.N.G.-J., I.J.B. and B.S.; Formal analysis, J.N.G.-J., I.J.B., B.S., M.-J.M. and C.K.; Investigation, J.N.G.-J., I.J.B. and B.S.; Methodology, J.N.G.-J., I.J.B. and B.S.; Project administration, J.N.G.-J. and I.J.B.; Resources, J.N.G.-J., I.J.B. and B.S.; Supervision, J.N.G.-J. and I.J.B.; Validation, J.N.G.-J., I.J.B. and B.S.; Visualization, J.N.G.-J. and B.S.; Writing—original draft, J.N.G.-J., I.J.B. and B.S.; Writing—review and editing, J.N.G.-J., I.J.B., B.S., M.-J.M. and C.K. All authors have read and agreed to the published version of the manuscript.

Funding: This research received no external funding.

Data Availability Statement: Publicly available datasets used in the structural re-interpretation of the Mt. Woods Inlier can be accessed through the South Australian Resource Information Gateway (SARIG) (https://map.sarig.sa.gov.au/ (accessed on 27 February 2019)).

Acknowledgments: The constructive reviews by two anonymous reviewers are gratefully acknowledged.

Conflicts of Interest: The authors declare that they have no known competing financial interests or personal relationships (conflicts of interest) that could have appeared to influence the work reported in this paper.

References

1. Schodde, R.C. Discovery performances of the western world gold industry over the period 1985–2003. In Proceedings of the PACRIM 2004 Congress, Adelaide, Australia, 19–22 September 2004; AUSIMM: Melbourne, Australia; pp. 367–380.
2. Hronsky, J.M.A.; Groves, D.I. Science of targeting: Definition, strategies, targeting and performance measurement. *Aust. J. Earth Sci.* **2008**, *55*, 3–12. [CrossRef]
3. Hrichi, S.; Chaabane-Banaoues, R.; Bayar, S.; Flamini, G.; Oulad El Majdoub, Y.; Mangraviti, D.; Mondello, L.; El Mzoughi, R.; Babba, H.; Mighri, Z.; et al. Botanical and Genetic Identification Followed by Investigation of Chemical Composition and Biological Activities on the *Scabiosa atropurpurea* L. Stem from Tunisian Flora. *Molecules* **2020**, *25*, 5032. [CrossRef]
4. Chauvet, A. Structural Control of Ore Deposits: The Role of Pre-Existing Structures on the Formation of Mineralised Vein Systems. *Minerals* **2019**, *9*, 56. [CrossRef]
5. Hobbs, B.; Zhang, Y.; Ord, A.; Zhao, C. Application of coupled deformation, fluid flow, thermal and chemical modelling to predictive mineral exploration. *J. Geochem. Explor.* **2000**, *69*, 505–509. [CrossRef]
6. Cox, S.F.; Knackstedt, M.A.; Braun, J. Principles of Structural Control on Permeability and Fluid Flow in Hydrothermal Systems. *Rev. Econ. Geol.* **2001**, *14*, 1–24. [CrossRef]
7. Sibson, R.H. Seismogenic framework for hydrothermal transport and ore deposition. *Rev. Econ. Geol.* **2001**, *14*, 25–50.
8. Oliver, N.H.S.; Ord, A.; Valenta, R.K.; Upton, P. Deformation, fluid flow and ore genesis in heterogeneous rocks, with examples and numerical models from the Mt Isa district, Australia. *Rev. Econ. Geol.* **2001**, *14*, 51–74.
9. Hildenbrand, T.G.; Berger, B.; Jachens, R.A.; Ludington, S. Regional Crustal Structures and Their Relationship to the Distribution of Ore Deposits in the Western United States, Based on Magnetic and Gravity Data. *Econ. Geol.* **2000**, *95*, 1583–1603. [CrossRef]
10. Robert, F.; Poulsen, K.H. Vein Formation and Deformation in Greenstone Gold Deposits. *Rev. Econ. Geol.* **2001**, *14*, 111–155. [CrossRef]
11. Ord, A.; Hobbs, B.E.; Zhang, Y.; Broadbent, G.C.; Brown, M.; Willetts, G.; Sorjonen-Ward, P.; Walshe, J.L.; Zhao, C. Geodynamic modeling of the century deposit, Mt Isa Province, Queensland. *Aust. J. Earth. Sci.* **2002**, *49*, 1011–1039. [CrossRef]
12. Zhang, Y.; Schaubs, P.M.; Zhao, C.; Ord, A.; Hobbs, B.E.; Barnicoat, A. Fault-related dilation, permeability enhancement, fluid flow and mineral precipitation patterns: Numerical models. In *The Internal Structure of Fault Zones: Implications for Mechanical and Fluid-Flow Properties*; Wibberley, C.A., Kurz, W., Imber, J., Holdsworth, R.E., Collettini, C., Eds.; Geological Society: London, UK, 2007; Volume 299, pp. 239–255.
13. De Roo, J.A. Structural controls on the emplacement of the vein-type tungsten-tin ore at Mount Carbine, Queensland, Australia. *Econ. Geol.* **1988**, *83*, 1170–1180. [CrossRef]
14. Groves, D.; Goldfarb, R.; Gebre-Mariam, M.; Hagemann, S.; Robert, F. Orogenic gold deposits: A proposed classification in the context of their crustal distribution and relationship to other gold deposit types. *Ore Geol. Rev.* **1998**, *13*, 7–27. [CrossRef]
15. Goldfarb, R.; Groves, D.; Gardoll, S. Orogenic gold and geologic time: A global synthesis. *Ore Geol. Rev.* **2001**, *18*, 1–75. [CrossRef]
16. Haest, M.; Muchez, P.; Dewaele, S.; Franey, N.; Tyler, R. Structural Control on the Dikulushi Cu-Ag Deposit, Katanga, Democratic Republic of Congo. *Econ. Geol.* **2007**, *102*, 1321–1333. [CrossRef]
17. Lawley, C.; Imber, J.; Selby, D. Structural Controls on Orogenic Au Mineralization During Transpression: Lupa Goldfield, Southwestern Tanzania. *Econ. Geol.* **2013**, *108*, 1615–1640. [CrossRef]
18. Koegelenberg, C.; Kisters, A.F.; Harris, C. Structural controls of fluid flow and gold mineralization in the easternmost parts of the Karagwe-Ankole Belt of north-western Tanzania. *Ore Geol. Rev.* **2016**, *77*, 332–349. [CrossRef]
19. Basson, I.; Thomas, S.; Stoch, B.; Anthonissen, C.; McCall, M.-J.; Britz, J.; Macgregor, S.; Viljoen, S.; Nel, D.; Vietze, M.; et al. The structural setting of mineralisation at Kolomela Mine, Northern Cape, South Africa, based on fully-constrained, implicit 3D modelling. *Ore Geol. Rev.* **2018**, *95*, 306–324. [CrossRef]
20. Gloyn-Jones, J.; Kisters, A. Regional folding, low-angle thrusting and permeability networks: Structural controls of gold mineralization in the Hope reef at Fairview Mine, Barberton Greenstone Belt, South Africa. *Ore Geol. Rev.* **2018**, *102*, 585–603. [CrossRef]
21. Gloyn-Jones, J.; Kisters, A. Ore-shoot formation in the Main Reef Complex of the Fairview Mine—multiphase gold mineralization during regional folding, Barberton Greenstone Belt, South Africa. *Miner. Depos.* **2019**, *54*, 1157–1178. [CrossRef]
22. Cathles, L.M. Fluid flow and genesis of hydrothermal ore deposits. *Econ. Geol.* **1981**, *75*, 424–457.
23. Cox, S.F. Coupling between deformation, fluid pressures, and fluid flow in ore-producing hydrothermal systems at depth in the crust. In *Economic Geology One Hundredth Anniversary Volume*; Hedenquist, J.W., Thompson, J.F.H., Goldfarb, R.J., Richards, J.P., Eds.; Society of Economic Geologists: Littleton, CO, USA, 2005; pp. 39–76.
24. Chi, G.; Xue, C. An overview of hydrodynamic studies of mineralization. *Geosci. Front.* **2011**, *2*, 423–438. [CrossRef]
25. Oliver, N.H.S. Review and classification of structural controls on fluid flow during regional metamorphism. *J. Metamorph. Geol.* **1996**, *14*, 477–492. [CrossRef]
26. Schlegel, T.; Heinrich, C.A. Lithology and Hydrothermal Alteration Control the Distribution of Copper Grade in the Prominent Hill Iron Oxide-Copper-Gold Deposit (Gawler Craton, South Australia). *Econ. Geol.* **2015**, *110*, 1953–1994. [CrossRef]

27. Schlegel, T.U.; Wagner, T.; Wälle, M.; Heinrich, C. Hematite-breccia hosted iron oxide–copper–gold deposits require magmatic fluid components exposed to atmospheric oxidation: Evidence from Prominent Hill, Gawler craton, South Australia. *Econ. Geol.* **2018**, *113*, 597–644. [CrossRef]
28. Reid, A. The Olympic Cu-Au Province, Gawler Craton: A Review of the Lithospheric Architecture, Geodynamic Setting, Alteration Systems, Cover Successions and Prospectivity. *Minerals* **2019**, *9*, 371. [CrossRef]
29. Hand, M.; Reid, A.; Jagodzinski, L. Tectonic Framework and Evolution of the Gawler Craton, Southern Australia. *Econ. Geol.* **2007**, *102*, 1377–1395. [CrossRef]
30. Hayward, N.; Skirrow, R.G. Geodynamic setting and controls on iron oxide Cu-Au (U) Ore in the Gawler Craton, South Australia. In *Hydrothermal Iron Oxide Copper—Gold and Related Deposits: A Global Perspective: Advances in the Understanding of IOCG Deposits*; Porter, T.M., Ed.; PGC Publishing: Linden Park, Australia, 2010; Volume 3, pp. 119–146.
31. Hronsky, J.M.A.; Groves, D.I.; Loucks, R.R.; Begg, G.C. A unified model for gold mineralization in accretionary orogens and implications for regional-scale exploration targeting method. *Min. Depos.* **2012**, *47*, 339–358. [CrossRef]
32. Tiddy, C.J.; Betts, P.G.; Neumann, M.R.; Murphy, F.C.; Stewart, J.R.; Giles, D.; Sawyer, M.; Freeman, H.; Jourdan, F. Interpretation of a ca. 1600–1580 Ma metamorphic core complex in the northern Gawler Craton, Australia. *Gondwana Res.* **2020**, *85*, 263–290. [CrossRef]
33. Skirrow, R.G.; Van Der Wielen, S.E.; Champion, D.C.; Czarnota, K.; Thiel, S. Lithospheric Architecture and Mantle Metasomatism Linked to Iron Oxide Cu-Au Ore Formation: Multidisciplinary Evidence from the Olympic Dam Region, South Australia. *Geochem. Geophys. Geosystems* **2018**, *19*, 1–33. [CrossRef]
34. Drexel, J.F.; Preiss, W.V.; Parker, A.J. The Geology of South Australia: Volume 1, The Precambrian. In *Geological Survey of South Australia 54*; Mines and Energy, South Australia, Geological Survey of South Australia: Adelaide, Australia, 1993; Volume 1.
35. Daly, S.J.; Fanning, C.M.; Fairclough, M.C. Tectonic evolution and exploration potential of the Gawler Craton, South Australia. *ASGO J. Aust. Geol. Geophys.* **1998**, *17*, 145–168.
36. Ferris, G.M.; Schwarz, M.P.; Heithersay, P. The geological framework, distribution and controls of Fe-oxide and related alteration, and Cu-Au mineralization in the Gawler Craton, South Australia. Part I: Geological and tectonic framework. In *Hydrothermal Iron Oxide Copper-Gold and Related Deposits: A Global Perspective*; Porter, T.M., Ed.; PGC Publishing: Adelaide, Australia, 2002; pp. 9–31.
37. Fanning, C.M.; Reid, A.J.; Teale, G. *A Geochronological Framework for the Gawler Craton, South Australia*; Mineral Resources Group, Division of Minerals and Energy Resources, Primary Industries and Resources South Australia: Adelaide, Australia, 2007.
38. Thiel, S.; Heinson, G.; White, A. Tectonic evolution of the southern Gawler Craton, South Australia, from electromagnetic sounding. *Aust. J. Earth Sci.* **2005**, *52*, 887–896. [CrossRef]
39. Betts, P.G.; Giles, D. The 1800–1100Ma tectonic evolution of Australia. *Precambrian Res.* **2006**, *144*, 92–125. [CrossRef]
40. Fraser, G.L.; Lyons, P. Timing of Mesoproterozoic tectonic activity in the northwestern Gawler Craton constrained by 40Ar/39Ar geochronology. *Precambrian Res.* **2006**, *151*, 160–184. [CrossRef]
41. Howard, K.; Reid, A.; Hand, M.; Barovich, K.; Belousova, E.A. Does the Kalinjala shear zone represent a paleosuture zone? Implications for distribution and styles of Mesoproterozoic mineralisation in the Gawler craton. *Min. Energy S. Aust. J.* **2006**, *43*, 6–11.
42. Hall, J.W.; Glorie, S.; Reid, A.J.; Collins, A.S.; Jourdan, F.; Danišík, M.; Evans, N. Thermal history of the northern Olympic Domain, Gawler Craton; correlations between thermochronometric data and mineralizing systems. *Gondwana Res.* **2018**, *56*, 90–104. [CrossRef]
43. Parker, A.J. Precambrian Provinces of South Australia—Tectonic setting. In *Geology of the Mineral Deposits of Australia and Papua New Guinea*; Hughes, F.E., Ed.; AUSIMM: Melbourne, Australia, 1990; pp. 985–990.
44. Fanning, C.M. *Ion-microscope U-Pb Zircon Dating of the Mount Woods Inlier, Preliminary Results*; Research School of Earth Science, Australian National University: Canberra, Australia, 1993, *unpub*.
45. Finlay, J. Structural Interpretation of the Mount Woods Inlier. Honours Thesis, Monash University, Melbourne, Australia, 1993.
46. Betts, P.G.; Valenta, R.; Finlay, J. Evolution of the Mount Woods Inlier, northern Gawler Craton, Southern Australia: An integrated structural and aeromagnetic analysis. *Tectonophysics* **2003**, *366*, 83–111. [CrossRef]
47. Holm, O. New geochronology of the Mount Woods Inlier and the central Gawler gold province. In *Gawler Craton: State of Play 2004, Conference Abstracts, Report Book 2004/18*; Department of Primary Industries and Resources South Australia: Adelaide, Australia, 2004.
48. Chalmers, N. *Mount Woods Domain: Proterozoic Metasediments and Intrusives*; Department of Primary Industries and Resources Report Book 2007/7: Adelaide, Australia, 2007.
49. Jagodzinski, E.A.; Reid, A.J.; Chalmers, N.; Swain., G.; Frew, R.A.; Foudoulis, C. *Compilation of SHRIMP U-Pb Geochronological Data for the Gawler Craton, South Australia*; Department of Primary Industries and Resources Report Book: Adelaide, Australia, 2007.
50. Forbes, C.; Giles, D.; Hand, M.; Betts, P.; Suzuki, K.; Chalmers, N.; Dutch, R. Using P–T paths to interpret the tectonothermal setting of prograde metamorphism: An example from the northeastern Gawler Craton, South Australia. *Precambrian Res.* **2011**, *185*, 65–85. [CrossRef]
51. Forbes, C.; Giles, D.; Jourdan, F.; Sato, K.; Omori, S.; Bunch, M. Cooling and exhumation history of the northeastern Gawler Craton, South Australia. *Precambrian Res.* **2012**, *200*, 209–238. [CrossRef]
52. Flint, R.B.; Benbow, M.C. *Geology of the Mount Woods Inlier*; Department of Mines, South Australia Report Book 77/134; Department for Energy and Mining: Adelaide, Australia, 1977; 50p.

53. Ambrose, G.J.; Flint, R.B. Billa Kalina South Australia Sheet SH53-7. Available online: https://sarigbasis.pir.sa.gov.au/WebtopEw/ws/plans/sarig1/image/DDD/200471-007 (accessed on 17 May 2022).
54. Parker, A.J.; Lemon, N.M. Reconstruction of the early Proterozoic stratigraphy of the Gawler Craton, South Australia. *J. Geol. Soc. Aust.* **1982**, *29*, 221–238. [CrossRef]
55. Vassallo, J.J. Structural repetition of the Hutchison Group metasediments, Eyre Peninsula, South Australia. *Aust. J. Earth Sci.* **2001**, *48*, 331–345. [CrossRef]
56. Fanning, C.M. *Geochronological Synthesis of South Australia. Part II: The Gawler Craton*; Unpublished PRISE Report; Research School of Earth Sciences, Australian National University: Canberra, Australia, 1997.
57. Belperio, A.; Flint, R.; Freeman, H. Prominent Hill: A Hematite-Dominated, Iron Oxide Copper-Gold System. *Econ. Geol.* **2007**, *102*, 1499–1510. [CrossRef]
58. Fanning, C.M.; Flint, R.B.; Parker, A.J.; Ludwig, K.R.; Blissett, A.H. Refined Proterozoic evolution of the Gawler Craton, South Australia, through U-Pb zircon geochronology. *Precambrian Res.* **1988**, *40*, 363–386. [CrossRef]
59. Johnson, J.P.; Cross, K.C. U-Pb geochronological constraints on the genesis of the Olympic Dam Cu-U-Au-Ag deposit, South Australia. *Econ. Geol.* **1995**, *90*, 1046–1063. [CrossRef]
60. Jagodzinski, E.A. *Compilation of SHRIMP U-Pb Geochronological Data for Zircons from Mafic Rocks of the Olympic Domain, Gawler Craton, South Australia, 2001–2003*; Geoscience Australia: Canberra, Australia, 2005.
61. Reeves, C. *Aeromagnetic Surveys Principles, Practice and Interpretation*; Earthworks, Geosoft: Washington, DC, USA, 2005.
62. Siddorn, J.P. *The Geological Interpretation of Aeromagnetic Data: A Geologist's Perspective*; KEGS Symposium: Toronto, ON, Canada, 2010.
63. Siddorn, J.P. Interpreting Aeromagnetic Data for Geological and Structural Mapping in the QUEST Area. In *Exploration Undercover: A Practical Example Using the QUEST Study Area*; Geoscience BC: Vancouver, BC, Canada, 2011.
64. Fullagar, P.K.; Pears, G.A. *Geologically Constrained Gravity and Magnetic Interpretation at Prominent Hill, South Australia. Internal Company Report for Robert Smith of Greenfields Geophysics*; Representing Oxiana Ltd.: Melbourne, Australia, 2007.
65. Tomkinson, M. *Preliminary Geological Domain Analysis, Southern Mount Woods Inlier, South Australia*; Epigenesis Consulting Pty Ltd.: Hillarys, Australia, 2007.
66. Tomkinson, M. *Observations on the Geology of the Southern Mount Woods Inlier including the "White Hills Complex"—Lithologies, Intrusions, Iron Oxide Textures and Possible Tectonic Setting*; Epigenesis Consulting Pty Ltd.: Hillarys, Australia, 2008.
67. Hill, R. *Eagle Project—Prominent Hill-GeoTEM Airborne Electromagnetics*; Four Winds Technology: New South Wales, Australia, 2008.
68. Betts, P.G. *Geophysical Interpretation Mount Woods Inlier*; PGN Geoscience: Melbourne, Australia, 2009.
69. Van der Wielen, S.E.; Fabris, A.J.; Halley, S.W.; Keeling, J.L.; Mauger, A.J.; Gordon, G.A.; Keeping, T.; Giles, D.; Hill, S.M. An exploration strategy for IOCG mineral systems under deep cover. *MESA J.* **2013**, *71*, 18–30.
70. Gale, K.; Anderson, I.; Harris, T.M. *Combined Annual Technical Report for the Period 1 January 2011 to 31 December 2011*; OZ Minerals: Adelaide, Australia, 2012.
71. Hossain, M.; Urosevic, M.; Kepic, A. Volumetric Interpretation of 3D Seismic Data from the Hillside IOCG Deposit in South Australia. In Proceedings of the 76th EAGE Conference and Exhibition, Amsterdam, The Netherlands, 16–19 June 2014.
72. Katona, L.F.; Wise, T.; Reid, A. *Vectorization of Residual Gravity and TMI Data in the Northern Gawler Craton: Implications for Exploration Targeting and GIS Analysis*; Geological Survey of South Australia: Adelaide, Australia, 2018. [CrossRef]
73. Korsch, R.; Kositcin, N.; Blewitt, R.S.; Fraser, G.L.; Baines, G.; Kennett, B.L.N.; Neumann, N.L.; Reid, A.J.; Preiss, W.V.; Giles, D.; et al. *Geodynamic Implications for the Deep Seismic Reflection Line 08GA-OM1: Gawler Craton—Officer Basin-Musgrave Province—Amadeus Basin (GOMA), South Australia and Northern Territory*; Geoscience Australia Record: Adelaide, Australia, 2010; pp. 63–86.
74. Harris, T.M.; Murphy, F.C.; Funk, C.W.; Betts, P.G. Mt Woods 2D Seismic Reflection Survey, Gawler Craton, South Australia: An Integrated Minerals Exploration Case Study. *ASEG Ext. Abstr.* **2013**, *2013*, 1–4. [CrossRef]
75. Wingate, M.T.; Campbell, I.H.; Compston, W.; Gibson, G.M. Ion microprobe U–Pb ages for Neoproterozoic basaltic magmatism in south-central Australia and implications for the breakup of Rodinia. *Precambrian Res.* **1998**, *87*, 135–159. [CrossRef]
76. De Little, J.; Gale, K.; Funk, C. *Combined Annual Technical Report for the Period 1 January 2009 to 31 December 2009*; OZ Minerals: Adelaide, Australia, 2010.
77. Gale, K.; Say, M.; Funk, C. *Combined Annual Technical Report for the Period 1 January 2010 to 31 December 2010*; OZ Minerals: Adelaide, Australia, 2011.
78. Groves, D.I.; Goldfarb, R.J.; Santosh, M. The conjunction of factors that lead to formation of giant gold provinces and deposits in non-arc settings. *Geosci. Front.* **2015**, *7*, 303–314. [CrossRef]
79. Hitzman, M.W.; Oreskes, N.; Einaudi, M.T. Geological characteristics and tectonic setting of Proterozoic iron oxide (Cu-U-AuREE) deposits. *Precambrian Res.* **1992**, *58*, 241–287. [CrossRef]
80. Belperio, A.P.; Freeman, H. Common geological characteristics of Prominent Hill and Olympic Dam—implications for iron oxide copper gold exploration models. In Proceedings of the PACRIM 2004, Adelaide, Australia, 19–22 September 2004; pp. 115–125.
81. Schlegel, T.U.; Wagner, T.; Heinrich, C.A.; Boyce, A.J. Magmatic-hydrothermal sulfur source for Prominent Hill and other iron oxide-copper-gold mineralisations in the Olympic IOCG province, South Australia. *Ore Geol. Rev.* **2017**, *89*, 1058–1090. [CrossRef]

82. Haddad-Martim, P.M.; Carranza, E.J.M.; de Souza Filho, C.R. The Fractal Nature of Structural Controls on Ore Formation: The Case of the Iron Oxide Copper-Gold Deposits in the Carajás Mineral Province, Brazilian Amazon. *Econ. Geol.* **2018**, *113*, 1499–1524. [CrossRef]
83. Carvalho, E.R. Caracterização Geológica e Gênese das Mineralizações de Óxido de Fe-Cu-Au e Metais Associados na Província Mineral de Carajás: Estudo de Caso do Depósito de Sossego. Ph.D. Thesis, Universidade Estadual de Campinas, Campinas, Brazil, 2009, *unpublished*.
84. Domingos, F.H.G. The Structural Setting of the Canaã dos Carajás Region and Sossego-Sequeirinho Deposits, Carajás, Brazil. Ph.D. Thesis, University of Durham, Durham, England, 2009, *unpublished*.
85. Vearncombe, J.R.; Holyland, P.W. Rheology, stress-mapping, and hydrothermal mineralization—The example of structurally-controlled gold-antimony deposits in South Africa. *S. Afr. J. Geol.* **1995**, *98*, 415–429.
86. Cundall, P.A.; Strack, O.D.L. A discrete numerical model for granular assemblies. *Géotechnique* **1979**, *29*, 47–65. [CrossRef]
87. Clough, R.W. The finite element method in plane stress analysis. In Proceedings of the Second ASCE Conference on Electronic Computation, Pittsburgh, PA, USA, 8–9 September 1960.
88. Zienkiewicz, O.C.; Taylor, R.L.; Zhu, J.Z. *The Finite Element Method: Its Basis and Fundamentals*; Butterworth Heinemann: Oxford, UK, 2013. [CrossRef]
89. Etheridge, M.A.; Wall, V.J.; Cox, S.; Vernon, R.H. High fluid pressures during regional metamorphism and deformation: Implications for mass transport and deformation mechanisms. *J. Geophys. Res. Earth Surf.* **1984**, *89*, 4344–4358. [CrossRef]
90. Oliver, N.H.S.; Valenta, R.K.; Wall, V.J. The effect of heterogeneous stress and strain on metamorphic fluid flow, Mary Kathleen, Australia, and a model for large-scale fluid circulation. *J. Metamorph. Geol.* **1990**, *8*, 311–331. [CrossRef]
91. Ridley, J. The relations between mean rock stress and fluid flow in the crust: With reference to vein- and lode-style gold deposits. *Ore Geol. Rev.* **1993**, *8*, 23–37. [CrossRef]
92. Ord, A.; Hobbs, B.E.; Zhao, C. Fundamentals of Computational Geoscience. In *Lecture Notes in Earth Sciences*; Springer: Berlin/Heidelberg, Germany, 2009; Volume 122. [CrossRef]
93. Sorjonen-Ward, P.; Zhang, Y.; Zhao, C. Numerical modelling of orogenic processes and gold mineralization in the southeastern part of the Yilgarn craton, western Australia. *Aust. J. Earth Sci.* **2002**, *49*, 1011–1039. [CrossRef]
94. Schaubs, P.M.; Rawling, T.J.; Dugdale, L.J.; Wilson, C.J.L. Factors controlling the location of gold mineralisation around basalt domes in the stawell corridor: Insights from coupled 3D deformation-fluid-flow numerical models. *Aust. J. Earth Sci.* **2006**, *53*, 841–862. [CrossRef]
95. Zhang, Y.; Lin, G.; Roberts, P.; Ord, A. Numerical modelling of deformation and fluid flow in the Shuikoushan district, Hunan Province, South China. *Ore Geol. Rev.* **2007**, *31*, 261–278. [CrossRef]
96. Zhang, Y.; Robinson, J.; Schaubs, P. Numerical modelling of structural controls on fluid flow and mineralization. *Geosci. Front.* **2011**, *2*, 449–461. [CrossRef]
97. Potma, W.; Roberts, P.A.; Schaubs, P.M.; Sheldon, H.A.; Zhang, Y.; Hobbs, B.E.; Ord, A. Predictive targeting in Australian orogenic-gold systems at the deposit to district scale using numerical modelling. *Aust. J. Earth Sci.* **2008**, *55*, 101–122. [CrossRef]
98. Wise, T.; Fabris, A.; Pridmore, D.; Reid, A.; Van Der Wielen, S.; Heinson, G.; Jakica, S.; Ziramov, S.; Soeffky, P. Olympic Dam seismic revisited: Reprocessing of deep crustal seismic data using partially preserved amplitude processing. *ASEG Ext. Abstr.* **2016**, *1*, 1–7. [CrossRef]
99. Edmond, J.; Paterson, M. Volume changes during the deformation of rocks at high pressures. *Int. J. Rock Mech. Min. Sci. Géoméch. Abstr.* **1972**, *9*, 161–182. [CrossRef]
100. Ord, A. Deformation of rock: A pressure-sensitive, dilatant material. *Pure Appl. Geophys.* **1991**, *137*, 337–366. [CrossRef]
101. Riley, S.J.; De Gloria, S.D.; Elliot, R. A terrain ruggedness index that quantifies topographic heterogeneity. *Intermt. J. Sci.* **1999**, *5*, 23–27.
102. Bowden, B.; Fraser, G.; Davidson, G.J.; Meffre, S.; Skirrow, R.; Bull, S.; Thompson, J. Age constraints on the hydrothermal history of the Prominent Hill iron oxide copper-gold deposit, South Australia. *Miner. Depos.* **2016**, *52*, 863–881. [CrossRef]
103. Christensen, D. In Proceedings of the New Copper Discovery in the Olympic Dam Copper Belt), Australian Copper Conference 2014, Brisbane, Australia, 17–18 June 2014.
104. Hronsky, J.M.; Kreuzer, O.P. Applying spatial prospectivity mapping to exploration targeting: Fundamental practical issues and suggested solutions for the future. *Ore Geol. Rev.* **2019**, *107*, 647–653. [CrossRef]